Tectonophysics 680 (2016) 192–210

Contents lists available at ScienceDirect

Tectonophysics

journal homepage: www.elsevier.com/locate/tecto

Tectonics, magmatism and paleo-fluid distribution in a strike-slip setting: Insights from the northern termination of the Liquiñe–Ofqui fault System, Chile

Pamela Pérez-Flores [a,b,*], José Cembrano [a,b], Pablo Sánchez-Alfaro [b,c], Eugenio Veloso [a,b], Gloria Arancibia [a,b], Tomás Roquer [a,b]

[a] Departamento de Ingeniería Estructural y Geotécnica, Pontificia Universidad Católica de Chile, Avenida Vicuña Mackenna 4860, Macul, Santiago, Chile
[b] Andean Geothermal Center of Excellence (CEGA, FONDAP-CONICYT), Santiago, Chile
[c] Departamento de Geología, Universidad de Chile, Santiago, Chile

ARTICLE INFO

Article history:
Received 26 December 2015
Received in revised form 30 April 2016
Accepted 10 May 2016
Available online 13 May 2016

Keywords:
Liquiñe–Ofqui Fault System (LOFS)
Andean Transverse Faults (ATF)
Strain partitioning
Fault-slip data inversion
Stress field
Magma/fluid transport

ABSTRACT

This study addresses the interplay between strain/stress fields and paleo-fluid migration in the Southern Andean Volcanic Zone (SVZ). The SVZ coexists with the margin-parallel Liquiñe–Ofqui Fault System (LOFS) and with NW-striking Andean Transverse Faults (ATF). To tackle the role of different fault-fracture systems on deformation distribution and magma/fluid transport, we map the nature, geometry and kinematics of faults, veins and dikes at various scales.

Fault-slip data analysis yields stress and strain fields from the full study area data base (regional scale) and fault zones representative of each fault system (local scale). Regional scale strain analysis shows kinematically heterogeneous faulting. Local strain analyses indicate homogeneous deformation with NE-trending shortening and NW-trending extension at NNE-striking Liquiñe–Ofqui master fault zones. Strain axes are clockwise rotated at second order fault zones, with ENE-trending shortening and NNW-trending stretching. The ATF record polyphasic deformation. Conversely, stress field analysis at regional scale indicates a strike-slip dominated transpressional regime with N64°E-trending σ_1 and N30°W-trending σ_3. Deformation is further partitioned within the arc through NNE-striking dextral-reverse faults, NE-striking dextral-normal faults and NW-striking sinistral-reverse faults with normal slip activation. The regional tectonic regime controls the geometry of NE-striking dikes and volcanic centers. NE-striking faults record local stress axes that are clockwise rotated with respect to the regional stress field. NNE- and NE-striking faults are favorably oriented for reactivation under the regional stress field and show poorly-developed damage zones. Conversely, NW-striking fault systems, misoriented under the regional stress field, show multiple fault cores, wider damage zones and dense vein networks.

Deformation driven by oblique subduction is partially partitioned into strike-slip and shortening components. The trench-parallel component is mostly accommodated by NS-striking right-lateral faults of the LOFS. Trench-perpendicular shortening is accommodated by sinistral-reverse ATF and dextral-reverse NNE-striking faults. We conclude that the SVZ records a deformation history coeval with magma/fluid migration.

1. Introduction

Bulk transpressional deformation is expected at continental margins where oblique convergence dominates (e.g. Dewey et al., 1998; Fossen and Tikoff, 1998; Sanderson and Marchini, 1984). Kinematic models show that transpressional deformation resulting from oblique convergence is accommodated by distinctive structural styles along and across to the overriding plate (Dewey et al., 1998; Federico et al., 2010; Fitch, 1972; Veloso et al., 2015). Strain in transpressional regimes can be partitioned into strike-slip and shortening components, depending mostly of the angle between the plate motion vector and the trench (convergence angle, α) and thermal constraints (Blanquat et al., 1998; e.g. Fossen et al., 1994; Teyssier et al., 1995; Tikoff and Greene, 1997). Large convergence angles ($20° < \alpha < 90°$) favor a pure-shear-dominated transpression with no strike-slip partitioning as is observed at Australian–Pacific plate boundary in New Zealand (e.g. Jarrard, 1986; Mccaffrey, 1992; Teyssier et al., 1995). In contrast, low convergence angle ($\alpha \leq 20°$) favor a strike-slip partitioned system, as in the case of wrench-dominated transpression at the Pacific–North America plate

* Corresponding author at: Departamento de Ingeniería Estructural y Geotécnica, Pontificia Universidad Católica de Chile, Avenida Vicuña Mackenna 4860, Macul, Santiago, Chile.
E-mail addresses: pvperez1@uc.cl (P. Pérez-Flores), jcembrano@ing.puc.cl (J. Cembrano), vsanchez@ing.uchile.cl (P. Sánchez-Alfaro), anveloso@ing.puc.cl (E. Veloso), garancibia@ing.puc.cl (G. Arancibia), teroquer@uc.cl (T. Roquer).

http://dx.doi.org/10.1016/j.tecto.2016.05.016
0040-1951/

boundary of the western US, where the San Andreas Fault takes up most of the simple shear component (e.g. Teyssier and Tikoff, 1998; Teyssier et al., 1995). The requirement of low angle of plate convergence is not applicable to magmatic arcs, where thermally weak intra-arc shear zones can accommodate a significant part of the bulk transpressional deformation by developing a trench-parallel fault system (Blanquat et al., 1998). Such intra-arc fault systems help to enhance crustal permeability as they host fault-fracture networks suitable for geothermal reservoirs, hydrothermal mineralization and/or volcanic activity (e.g. Caine et al., 1996; Cox, 1999; Micklethwaite and Cox, 2004; Rowland and Sibson, 2004; Sibson, 1994). During fault rupture, propagation of individual faults may develop an associated damage zone where discontinuous fracturing, dilatant sites and minor shears dominate and provide suitable places for storage of fluid-related materials (e.g. Connolly and Cosgrove, 1999; Sibson, 1996; Zhang et al., 2008). As such, fault-fracture systems are potential fluid pathways in the crust, which is otherwise relatively impermeable (e.g. Connolly and Cosgrove, 1999; Faulkner et al., 2010).

Numerical models, mechanical experiments and field observations reveal that damage zones enhance rock permeability acting as a conduits for hydrothermal fluid flow and magma migration (e.g. Cox, 1999; Curewitz and Karson, 1997; Gudmundsson et al., 2001; Mitchell and Faulkner, 2012; Sheldon and Micklethwaite, 2007; Zhang et al., 2008). In hydrothermal systems, episodic mineral precipitation seals both the intrinsic permeability related to the primary rock porosity as well as that related to fracture networks (Cox, 2010). Therefore, repeated reactivation of the fault-fracture network is required to maintain the permeability within the fracture controlled hydrothermal systems. Moreover, fault reactivation of pre-existing fault and opening of extension fractures networks or hybrid extensional–shear fractures (permeability regeneration) depends mainly on depth, rock mechanical properties, pore fluid pressure and the orientation of faults with respect to the maximum principal stress axis (Cox, 2010; Faulkner and Armitage, 2013; Moeck et al., 2009; Sibson, 2004, 2003, 1996).

Distinctive mineral textures observed on a variety of structural elements such as slickenfibers on fault surfaces, veins and fault-veins, suggest a direct link between these and the episodic fault reactivation or seismic cycle (e.g. Power and Tullis, 1989; Uysal et al., 2011). For example, dilational implosion breccia exhibiting evidences of hybrid (dilatant and shear deformation) are thought to represent co-seismic dilatancy and hydraulic connection with an ancient geothermal reservoir (Kolb et al., 2005; Melosh et al., 2014; Micklethwaite and Cox, 2004; Saul et al., 2010). Other specific mineral textures, such as lattice bladed or jigsaw calcite and silica, are thought to result from precipitation by boiling processes, indicating quick depressurization caused by space-opening (Moncada et al., 2012; Sibson et al., 1975; Uysal et al., 2011). Moreover, slickenfibers, a distinctive feature of fault-veins, are interpreted as episodic mineral growth at relatively low strain rate during the interseismic period (e.g. Power and Tullis, 1989) and/or as a fossil evidence of repeated microearthquakes (Fagereng et al., 2011).

Because magma also uses fault-fracture meshes as preferential conduits to migrate through the crust, the spatial distribution of intrusive bodies, dike swarms and volcanic centers record the regional and local stress fields (Acocella and Funiciello, 2006; Karaoğlu, 2014; Nakamura, 1977). Extension fractures develop perpendicular to the minimum principal stress axis (σ_3). Within fault-fracture meshes, the high permeability direction is developed parallel to the intermediate principal stress axis (σ_2), which is commonly parallel to fault-fracture intersections and orthogonal to fault slip vectors (Sibson, 1996).

Thus, the question arises as to how deformation partitioning across the overriding plate controls the hydrothermal and magmatic fluid migration pathways. A complete geologic and structural record present in the Southern Volcanic Zone (SVZ) provides an excellent natural laboratory to unravel the interactions between stress field variations within strike-slip settings, hydrothermal fluid permeability and magmatic emplacement (Fig. 1). The SVZ exposes a regional fault system parallel to the Andean belt, the Liquiñe–Ofqui Fault System (LOFS), and several Andean Transverse Faults (ATF) (called arc-oblique fault system by Sánchez et al., 2013). These structures have different geometry, kinematics and complex cross-cutting relationships (Cembrano and Lara, 2009; Chernicoff et al., 2002; Lara et al., 2006; Melnick et al., 2006a; Sánchez et al., 2013). In this study, we present the role of stress field variations at local scale on paleo-fluid/magma distribution at different fault-fracture orientations at the northern termination of Liquiñe–Ofqui fault system. We provide a comprehensive and integrated view of the interplay between regional/local stress field orientation and fault-fracture meshes in an intra-arc transpressional setting.

2. Geological background

2.1. Structural setting

Oblique convergence between the Nazca and South America plates is the driving mechanism for the stress distribution and deformation pattern imposed on the overriding plate (Beck, 1988; Cembrano et al., 2000, 1996). For the southernmost part of South America, the convergence angle (α) ranges between 64° and 70° over the last 10 Ma (Fig. 1b) (e.g. Pardo-Casas and Molnar, 1987; Cande and Leslie, 1986). GPS data indicates that present-day convergence velocity of the Nazca oceanic plate is about 66 mm/year, with a subduction angle of ca. 20° (Angermann et al., 1999).

Part of the deformation imposed by oblique plate motion is accommodated in the intra-arc Liquiñe–Ofqui Fault System (LOFS) (Fig. 1) (e.g. Arancibia et al., 1999; Cembrano and Herve, 1993; Cembrano and Lara, 2009; Lavenu and Cembrano, 1999). Thus, as a result of the subduction process, the forearc and intra-arc zones document changes on the degree of deformation partitioning, along and across the Southern Andes (Arancibia et al., 1999; Lavenu and Cembrano, 1999; Rosenau et al., 2006).

The LOFS is 1200 km-long intra-arc strike-slip fault system, which is defined by a series of major NNE-striking, right-lateral, strike-slip faults associated with NE-striking normal-dextral faults that splay off NNE-striking faults. This spatial arrangement forms duplexes and horsetail geometries at both ends of the fault system (Fig. 1) (Cembrano and Lara, 2009; Rosenau et al., 2006). The LOFS partially controls the occurrence, spatial distribution and geometry of major stratovolcanoes (Cembrano and Lara, 2009; Lara et al., 2008; Melnick et al., 2006a; Sielfeld et al., 2016) (Fig. 1). The LOFS records right-lateral ductile deformation between 6 and 3 Ma (Cembrano et al., 2000) that is crosscut by dextral brittle deformation since 1.6 Ma (Lavenu and Cembrano, 1999). Present-day activity of this fault system would absorb about 6.5 mm/yr of northward motion of the forearc, as recorded by GPS (Wang et al., 2007) and widespread crustal seismicity (Fig. 1). Shallow (<25 km) seismic activity (Haberland et al., 2006; Lange et al., 2008) is present throughout the LOFS. At the southern termination of LOFS (Aysén Fjord) a seismic swarm occurred in April 2007 together with a *Mw* 6.2 earthquake at 12 km of depth, with a right-lateral focal mechanism at a NS-striking fault plane (Fig. 1a) (Legrand et al., 2011). Similarly, at the northern termination of LOFS, in December 2006 a *Mw* 5.5 earthquake at 18 km depth was recorded south of Callaqui volcano (Fig. 1b). The focal mechanism of this event (http://www.globalctm.org) can be attributable to right lateral NNE-striking fault slip or left lateral NW-striking fault slip, both faults are present in the area. At Lonquimay volcano (Fig. 1b), a *Mw*. 5.3 earthquake at 15 km of depth was recorded after two months of a flank cone eruption. The focal mechanism of this event is a right-lateral oblique slip in a NNE-striking fault (Barrientos and Acevedo-Aránguiz, 1992; Dziewonski et al., 1990). All of these events are compatible with ENE-shortening and NNW-extension.

The ATF, in turn, is formed by a series of discrete, NW-striking faults inherited from pre-Andean geological processes (Fig. 1a) (e.g. Radic, 2010). At the scale of the Andean Orogen, the faults that conform the ATF are spatially and genetically associated with the occurrence of several ore deposits (e.g. El Pescado, Cerro Guachi and Chuquicamata

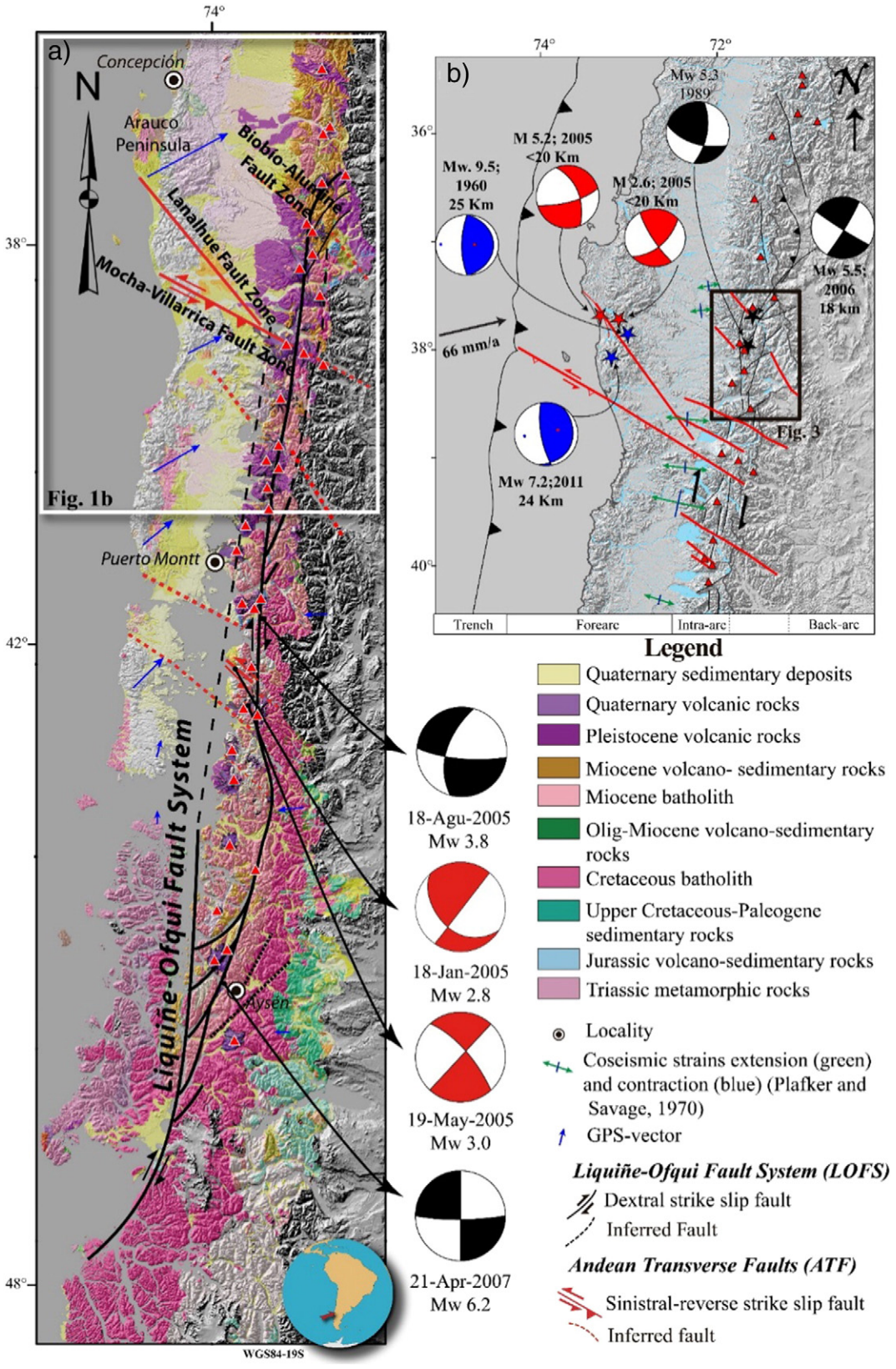

Fig. 1. (a) Composite Digital Elevation Model and 1:1,000,000 geological map of the Southern Andes Volcanic Zone (SVZ) (Sánchez et al., 2013). Regional map showing the location and extent of the LOFS (black lines), ATF (red lines) and main Holocene volcanoes (red triangles). Previously published focal mechanisms of crustal earthquakes are shown for the LOFS (black) and ATF (red) (Barrientos and Acevedo-Aránguiz, 1992; Lange et al., 2008; Legrand et al., 2011). A selection of GPS vectors is shown (Lin et al., 2013; Wang et al., 2007). (b) Digital Elevation Model showing the principal fault systems in southernmost Chile: LOFS (black line) and ATF (red line). Convergence velocity vector after Angermann et al. (1999). Subduction zone earthquakes (blue stars), ATF earthquakes (red stars) and LOFS earthquakes (black stars) are shown as well as their respective focal mechanisms (redrawn after Cifuentes, 1989; Haberland et al., 2006; Moreno et al., 2009). The coseismic shortening and extension axes calculated for 1960 earthquake are shown (Plafker and Savage, 1970).

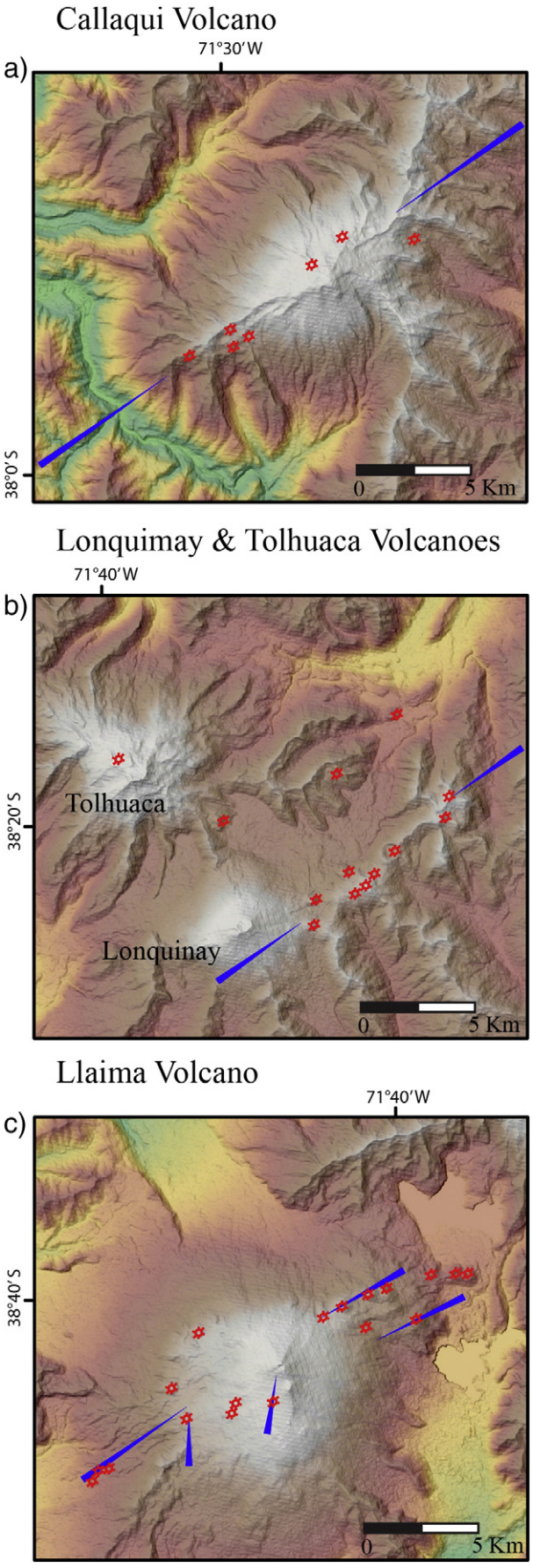

mines) (e.g. Chernicoff et al., 2002), cenozoic basins (e.g. Radic, 2010) and the segmentation of subduction earthquakes (Melnick et al., 2009). Furthermore, transverse faults are linked with Quaternary volcanism in the Central and Southern Andes (Fig. 1) (Acocella and Funiciello, 2006; Cembrano and Lara, 2009; Cembrano and Moreno, 1994; Lara et al., 2006, 2004; Sánchez et al., 2013; Tibaldi et al., 2005). Remote sensing, field observations and geophysical evidence (such as Vp/Vs tomography, magnetic anomalies, gravimetry and shallow seismicity) suggest that the faults of the ATF are deep-seated lithospheric-scale structural elements (Sánchez et al., 2013; Yáñez et al., 1998). The ATF partially control the past and present-day fluid flow, volcanic activity and shallow seismic activity (Haberland et al., 2006; Lara et al., 2006, 2004; Sánchez et al., 2013; Tardani et al., 2016). One of ATF (Pichilemu fault), recorded permanent extensional coseismic deformation in forearc after the *Mw* 8.8 Maule subduction earthquake in central Chile (35°S), including the *Mw* 6.9 and *Mw* 7.0 events at depths between 16 and 20 km WSW-trending extension axis (Aron et al., 2013). The Lanalhue fault (Fig. 1a), another transverse fault, recorded interseismic transpressional deformation of the forearc (38°S) including a M_L 5.2 at 12 km depth with a left-lateral focal mechanism (Fig. 1b) (Haberland et al., 2006). Within the study area, the expression of these series of faults is the so-called Biobio–Alumine Fault System (BAFS) (Fig. 1) (Melnick et al., 2006a; Muñoz and Stern, 1988) which is represented by a rectilinear, NW-trending valley filled with Quaternary fluvial deposits.

2.2. Geometry and spatial distribution of dikes and eruptive centers

At the northern termination of LOFS (Fig. 1b), flank vents and dikes are aligned along N60°E-trending orientations (e.g. Cembrano and Lara, 2009; López-Escobar et al., 1995). Associated eruptive products range from andesite to basalt, similar to the composition of dikes that locally feed eruptive vents (Sielfeld et al., 2016). Most of such flank vents are Holocene or younger (historical). At Callaqui volcano, flank vents ages are constrained from late-Pleistocene to Holocene and dikes ages are bracketed between 146 ± 30 ka and 77 ± 28 ka (^{40}Ar–^{39}Ar, basaltic groundmass) (Sielfeld et al., 2016). At Lonquimay volcano, there was a recent flank vent eruption on December 25th, 1988 (Navidad vent) (Fig 2b). At Llaima volcano, flank cones record three eruptions at 2008, 1957 and ~1850 (Bouvet de Maisonneuve et al., 2012). These young volcanic centers have been used to unravel the geometry and kinematics of underlying feeder fractures (e.g. Corazzato and Tibaldi, 2006; Nakamura, 1977; Van Wyk De Vries and Merle, 1998).

Morphological analysis of flank vents on several volcanoes at the SVZ shows the spatial distribution of their feeder fractures. For example, at Callaqui volcano, this analysis reveals a preferential NE-trending alignment of feeder fractures, consistent with the spatial distribution of spatially associated dyke systems. The dikes and flank vent distribution constitute the architecture of the NE-elongation of Callaqui volcano (Fig. 2a) (Sielfeld et al., 2016). Similarly, at Lonquimay and Llaima volcanoes, the distribution of flank vents suggests that feeder fractures have the same preferential orientation (N60E) (Fig. 2b and c, respectably) (Bertin, 2010; Bouvet de Maisonneuve et al., 2012).

3. Methodology

3.1. Field and laboratory structural geology

The study area is located between the Callaqui and Llaima volcanoes encompassing a region of about 150 km by 80 km in the main Andean

Fig. 2. Digital Elevation Models showing the preferential orientation of flank cones (red circles) and volcanic vents (blue lines) (Bertin, 2010; Bouvet de Maisonneuve et al., 2012; Maurice, 2012; Sielfeld et al., 2016) of the (a) Callaqui, (b) Lonquimay and Tolhuaca, (c) Llaima volcanoes.

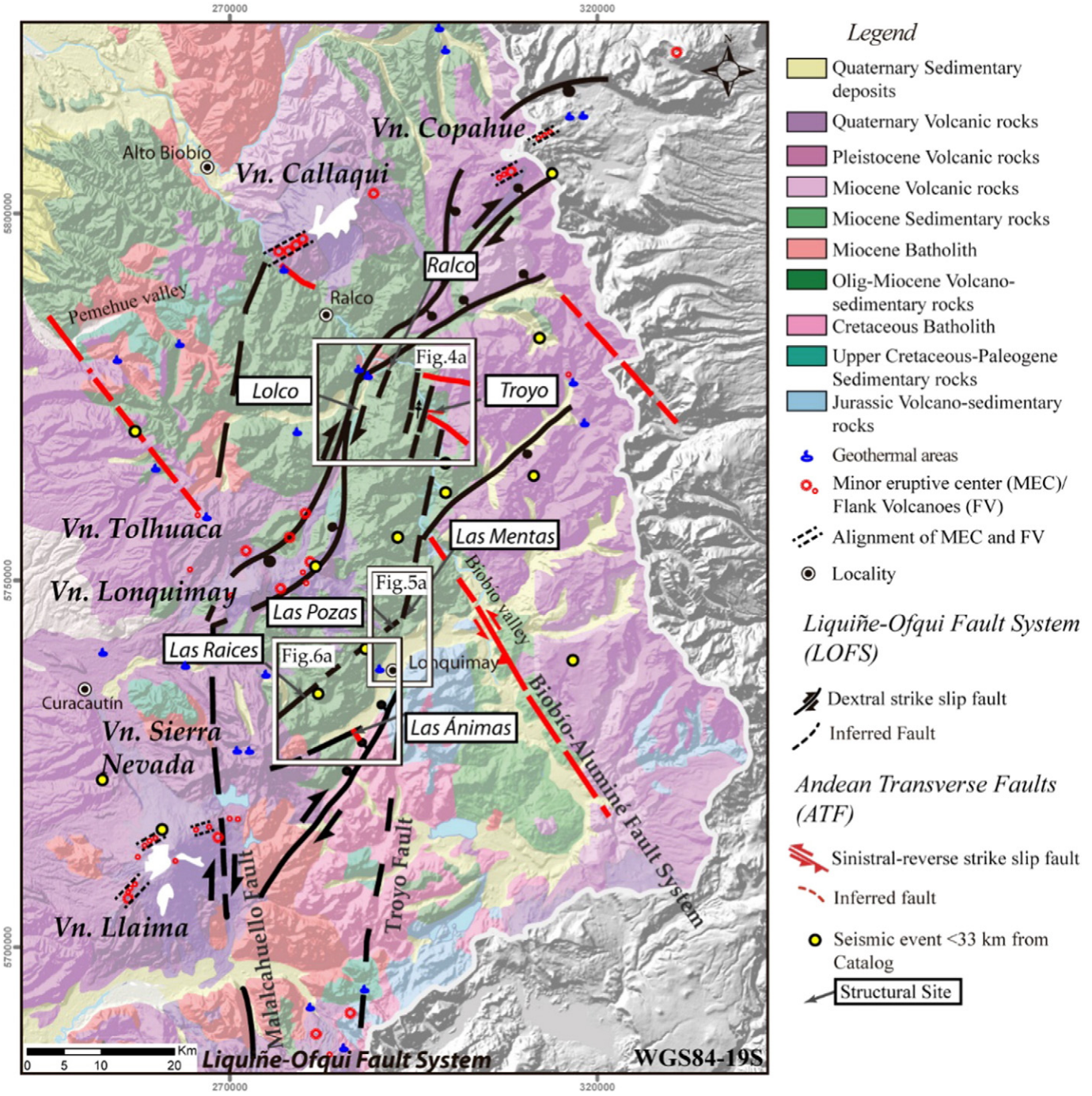

Fig. 3. Geological–structural map of the Southern Volcanic Zone of the Andes, between 37°30′S and 39°S (see location at Fig. 1b) showing the northern termination of the LOFS and the NW-striking faults belonging to ATF (red lines). The white squares show areas of detailed structural mapping sites.

Cordillera of southern Chile (Figs. 1b and 3). The major structural domains documented in this work were defined based on a combination of photointerpretation on Digital Elevation Models and quickbird images (from Google Earth), previous works (Melnick et al., 2006b; Rosenau et al., 2006; Suárez and Emparan, 1997; Thiele et al., 1987) and our field study from regional (1:50,000) to local (1:500) scales. We selected three representative areas for detailed structural mapping in order to characterize the geometry, kinematics and timing of deformation on structural domains of the LOFS and ATF as present in the study area (Fig. 3). Within these areas, we defined seven key structural sites, which are representative of LOFS and ATF fault zones; La Poza, Las Mentas, Ralco, Lolco, Las Raices, Las Animas structural sites (Table 1) (Figs. 3, 4a, 5a, 6a). Collected structural data include description, measurement and logging of the geometry, kinematics, texture, mineralogy and crosscutting relationship of different structural elements (i.e. fault-veins, veins, hydrothermal breccias). When kinematics or mineralogy was not clear at the outcrop scale, we performed microstructural analyses by using optical microscope. When mineral identification at hand and optical microscope scale was not possible, we used X-ray diffraction (XRD) and scanning electron microscope (SEM). XRD analyses were performed at the Laboratorio de Cristalografía of the Universidad de Chile using a Bruker D8 Advance X-Ray Diffractometer (radiation Cu Kα = 1.5406 Å), equipped with a Cu X-Ray tube (operating at 40 kV/30 mA), Ni filter, sample spinner and a solid-state detector (Lineal

Table 1
The table summarized the detail mapping at each structural site. The information displayed is the host rock age from closer data of Suárez and Emparan (1997) and main structural elements.

Structural site	Host rock	Age (Ma)	Structural element	Principal orientation	Mineralogy and texture	Strain solution				Stress solution			
						P	T	R	Strain ellipsoid	ϕ	σ_1	σ_3	Tectonic regime
Lolco (L). LOFS, first order	Andesite. Cura–Mallin Formation	13.1 ± 0.7 K–Ar Total rock	Dextral faults Veins and Hydrothermal breccia	NNE NE	Several centimetric faults with zeolite slickenfibers. 0.1–2.0 cm-thick, laumontite, fault-veins.	066/24	157/2	0.48	Plane-strain	0.40	066/21	335/02	Strike-slip
Ralco (R). LOFS, first order	Shale and sandstone. Cura–Mallin Formation	19.1 ± 2.8 K–Ar Total rock	Dextral faults Normal fault Veins Hydrothermal breccia	NNE NE NE NNE-NE intersection	Several, 0.2–1.0 cm-thick faults with calcite slickenfibers. Gauge fault core, 2 cm thick and 1 m offset. Syntaxial calcite, with high dip variability, usually parallel to shale lamination Mosaic breccia texture with bladed-like calcite.	237/57	329/01	0.27	Constrictional	0.50	041/43	138/07	Strike-slip
Troyo (T). LOFS, first order.	Andesite. Cura–Mallin Formation	14.1 ± 1.6 K–Ar Total rock	Dextral faults Sinistral faults Veins	NS WNW NE	Decametric, 20 cm thick and zeolite slickenfibers. 50 cm thick fault core with zeolite slickenfibers displaying Riedel-type shears fractures locally exhibiting hydrothermal breccia lenses. 0.2–1.0 cm-thick zeolite veins form dextral duplex.	167/61	311/25	0.56	Plain strain	0.70	211/23	312/25	Strike-slip transtensional
Las Mentas (LM). LOFS, first order.	Andesite. Cura–Mallin Formation	11.9 ± 0.8 K–Ar Total rock	Dextral deformed band Dextral-reverse faults Veins Sinistral-reverse faults Veins	NNE NS NE EW ENE to ESE	50 cm thick foliated band and S–C fabric. 10 cm gouge core fault 0.3–5 cm thick zeolite veins locally forming crackle breccia. Several centimetric faults with calcite slickenfibers 0.3–2.0 cm thick calcite filled with locally breccia lenses	208/75	332/9	0.74	Flattening	0.40	067/31	327/16	Strike-slip
La Poza (LP). LOFS, intersection first/s order	Andesite. Cura–Mallin Formation.	11.9 ± 0.8 K–Ar Total rock	Dextral faults Dextral-normal faults	NNE NE	Several 0.1–1.0 cm gouge thick fault cores. Decametric fault with 15–30 thick fault core, consist of gouge and fault breccia.	243/02	153/0	0.46	Plane strain	0.20	059/05	326/46	Strike-slip transpressional
Las Raices (LR). LOFS, second order.	Andesite.	19.9 ± 1.4 K–Ar Total rock	Dextral -reverse faults Normal-dextral faults Andesitic dikes Veins	NNE NE-ENE NE-ENE ENE	Several 0.5–2.0 cm thick faults with calcite slickenfibers. Decametric faults between 10 and 50 cm thick fault core with laumontite and stilbite veins and less calcite, locally form hydrothermal breccia lenses. 20 to 50 cm wide hosted throughout NE-ENE faults. Syntaxial stilbite veins 0.5–3.0 cm thick	261/02	352/19	0.56	Plane strain	0.20	078/32	346/03	Strike-slip transpressional
Las Animas (LA). ATF	Interlayer of andesite and hornblende andesite. Cura–Mallin Formation	–	Sinistral-reverse faults with reactivation of normal faults Hydrothermal breccias bodies Veins and hydrothermal breccias	NW NW-NE intersection NW-EW	Foliated fault cores between 30 and 50 cm wide. Asymmetric damage zone stronger at hanging wall. 1 m normal offset of marker layer and 0.2–1.0 cm reverse offsets inside of core fault, forming a gentle fault propagated anticline fold. Tabular bodies between 4 and 6 m wide which have transition from veins stockwork, crackle breccias and hydrothermal breccia consist of rounded clasts (10–30 cm diameter) with zeolite-calcite matrix. 0.2–15.0 cm wide, banded veins consist of stilbite edge and hydrothermal breccia center with laumontite matrix and locally calcite. 0.2–2 cm wide, stilbite veins.	– –	– –	– –	– –	0.90 0.60	227/45 110/19	356/32 011/22	Strike-slip transtensional Strike-slip

LynxEye). The resulting diffractograms were interpreted with the software package Match! by Crystal Impact, and compared with Panalytical-ICSD (Inorganic Crystal Structure Database) database. SEM analyses were performed in the University College London laboratory using a Jeol JSM-6480LV high-performance, Variable Pressure Analytical Scanning Electron Microscope with a high resolution of 3.0 nm, along with EDS (Energy Dispersive System) and EBSD (Electron Backscatter Diffraction) using the Oxford Link system.

3.2. Fault-slip data inversion

Structural data collected was analyzed from regional and local scales. The regional scale was defined by the inversion of the entered fault-slip data collected at the study area (Fig. 3), whereas for local scale the inversion is the results of fault-slip data of each structural site: Ralco, Lolco, Troyo, Las Mentas, Las Pozas, Las Raices and Las Animas structural sites (Fig. 3). Two different softwares were used to determine the strain and stress axes, Faultkin 7.4.1 and Multiple Inversion Method (MIM).

3.2.1. Determination of strain field

The software Faultkin 7.4.1 (Allmendinger et al., 2012; Marrett and Allmendinger, 1990) is a graphical and numerical technique that allows qualitative and quantitative kinematic analysis of fault-slip data by calculating the orientations of the maximum shortening (P) and the maximum stretching (T) axes associated with each individual fault plane. P- and T-axes are an integrated and alternative representation of the orientation and kinematics of a fault, since calculus of both axes requires knowledge of the orientation of the (fault) plane and of the displacement vector resolved on such (fault) plane (slickenline) (Marrett and Allmendinger, 1990). For a single fault-slip datum, the orientation of the P- and T-axes lies in the movement plane – defined by the maximum shear vector (striae) and the fault pole vector – at 45° to the pole vector (Marrett and Allmendinger, 1990). The main, or representative, orientations of both P and T axes for a given fault population are calculated assuming the data represents a uniform deformation field (spatially and temporally). In this case, the main P- and T-axes are calculated assuming that these are clustered following a statistical Bingham distribution. However, non-clustered P- and/or T-axes, indicate that the fault data population is the result of kinematically heterogeneous faulting, represented by girdle or multi-modal patterns of shortening and/or extension axes. Kinematic heterogeneity can arise from several causes, such as triaxial deformation, anisotropy reactivation, strain compatibility constraints and/or polyphasic deformations (Marrett and Allmendinger, 1990).

Because P and T axes are related to the orientation of the principal incremental strain axes, it is possible to measure the shape of the strain ellipsoid by using the ratio, $R = (E_2 - E_3)/(E_1 - E_3)$, where E_1, E_2 and E_3 are the eigenvalues of the Bingham moment tensor obtained for each clustered T, B and P axis respectively. R values equal to 1.00, 0.50 and 0.00 indicate ideal flattening, plane-strain and constrictional ellipsoids, respectively. In a general sense, and as pointed by Diraison et al. (2000), values between 0.00 and 0.35 indicate a constrictional type, while values between 0.35 and 0.65 indicate a plane strain type. Values in the range of 1.00–0.65 indicate a flattening type strain ellipsoid.

3.2.2. Determination of stress field

The "Multiple Inverse Method" (MIM) is based on a geometrical criterion (Yamaji, 2000), being a modification of the classic inverse technique of Angelier (1984). The method is capable of calculating and sorting the orientation of the principal stress axes derived from a heterogeneous fault-slip data set by generating a combinatorial amount of groups containing each *k*-number of fault-slip data elements extracted from the whole data set (Yamaji et al., 2005). Then it applies Angelier's (1984) inverse technique to all of these randomly generated subsets. Finally, the orientations of the calculated stress axes for each generated group of *k*-number fault-slip data are plotted onto separate stereograms: one for σ_1 axes and another for σ_3 axes sub-solutions (Otsubo et al., 2006; Yamaji, 2000). Each sub-solution is represented

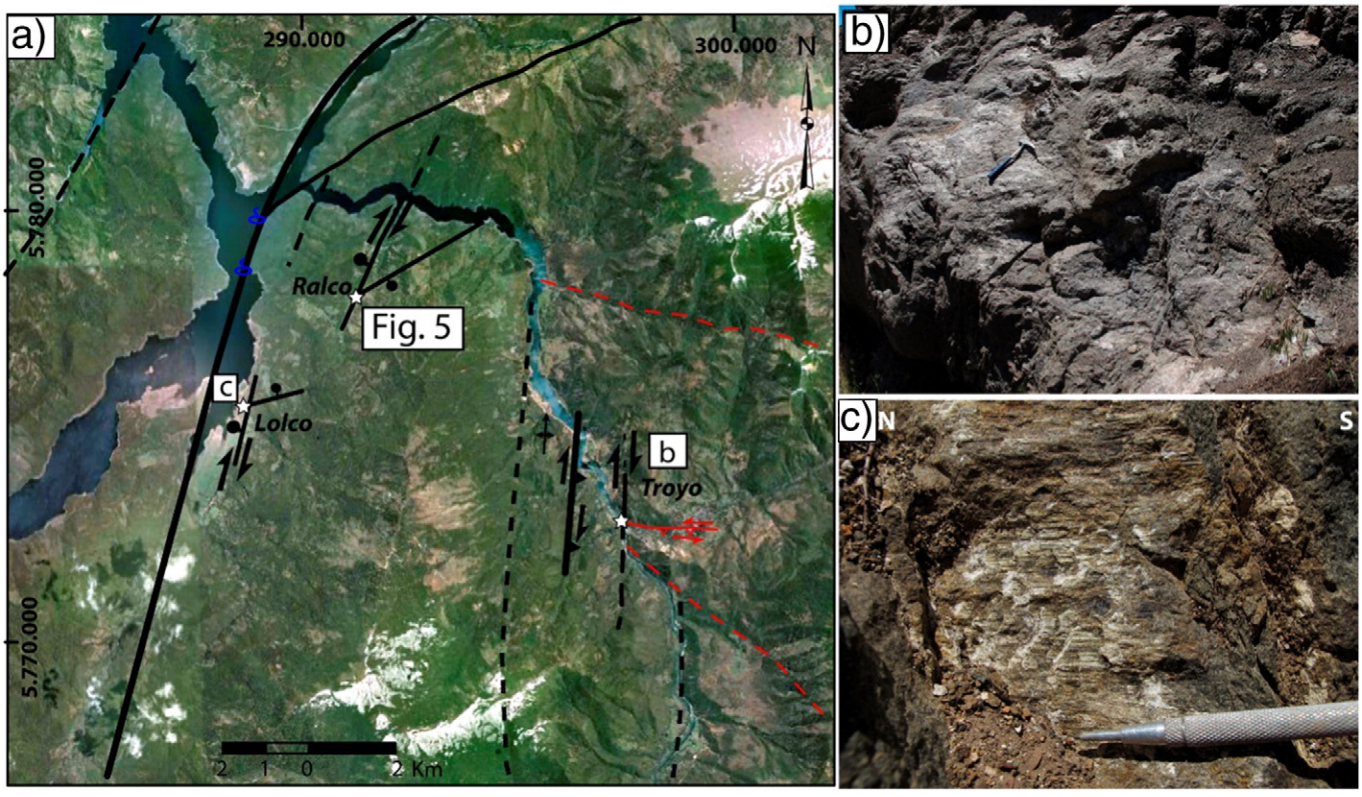

Fig. 4. (a) Google Earth image showing the Lolco, Ralco and Troyo structural sites. Panels b to c show examples of different structural elements seen in the field. (b) East-striking, shallowly-dipping, sinistral fault (N85°W/45°S rake:20°W); (c) N10°E-striking, steeply dipping, dextral fault with zeolite slickenfibers.

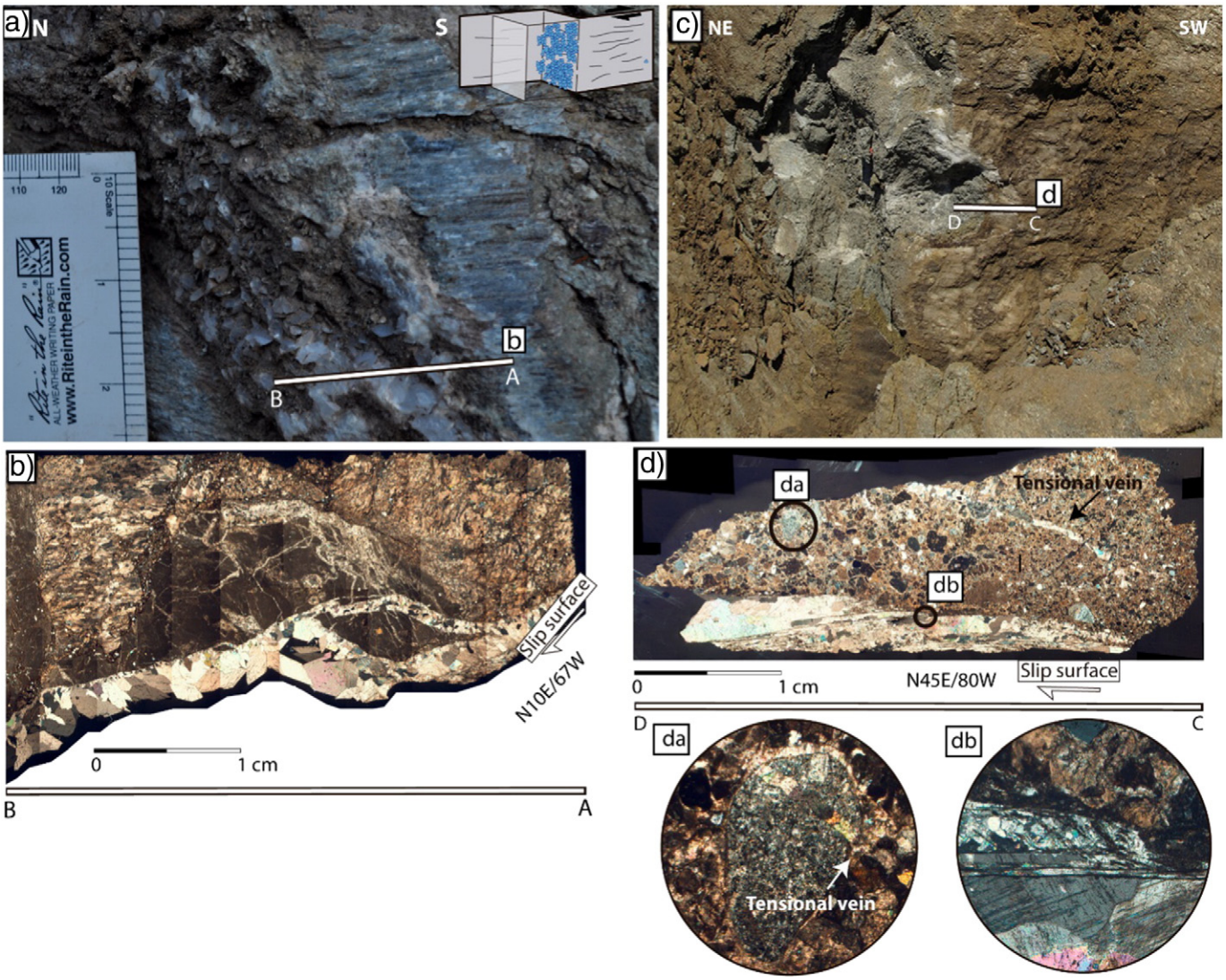

Fig. 5. See location in Fig. 4. (a) Dilatational jog between NNE and NE-striking dextral faults hosting bladed-like calcite; (b) oriented thin section perpendicular to the fault plane and parallel to striae showing calcite microstructure. Note that a sigmoidal piece of the wall rock is detached at the dilational site; (c) N60°E-striking fault with subhorizontal striae and dextral strike-slip kinematics; (d) oriented thin section photo-mosaic showing calcite slickenfibers sheets with sharp contact surfaces and a transitional texture from a brittle shear zone in the host rock contact (da) to blocky crystal types following the slip direction. (db) Extension fractures (N70°E) locally cut some clasts of the wall-rock.

as a tadpole indicating the orientation of one of the principal axes with an attached 'tail' pointing toward the orientation of the complementary principal axis (i.e., σ_1's tadpole points toward the orientation of σ_3 and vice versa). This symbol is, additionally, color-coded according to the calculated stress ratio ($\varphi = (\sigma_2 - \sigma_3) / (\sigma_1 - \sigma_3)$; $\varphi = 1 -$ stress shape ellipsoid (R)). Thus, groups of tadpoles with similar colors and similar orientations of their tails indicate a compatible stress field solution (Federico et al., 2010; Otsubo et al., 2006; Veloso et al., 2015, 2009; Yamaji, 2000). The distribution of φ-values is therefore used to establish a φ-value range for the principal stress axes solution. In the case where φ-histograms show a bimodal distribution, we calculated one field stress solution for each range of representative φ-values. Thus, for the field stress obtained, the misfit angle or difference between observed and theoretical slip direction obtained from an assumed stress state is calculated. The stress axes orientation solution is calibrated by choosing the solution with a bigger number of activated faults with misfit angles of less than 30°. Thus, the tectonic regime is defined by the principal stress axes orientation as extensional, compressional or strike-slip (Ritz, 1994). The strike-slip regime could be either transpressional or transtensional regimen depending of stress ratio value (φ). A $\varphi > 0.55$ represents a transtensional tectonic regime, $\varphi < 0.45$ represents a transpressional tectonic regime and $0.45 < \varphi < 0.55$ represent a simple shear dominated strike-slip tectonic regime (see detailed discussion about φ-value interpretation at Bellier and Zoback, 1995; Siame and Bellier, 2005).

4. Results

4.1. Architecture and geometry of fault fracture networks in the study area

Based on the detailed mapping at each structural site, the main features of structural elements are summarized in Table 1. Structural elements described in the study area are hosted by volcanic and sedimentary rocks belonging to the Cura–Mallin Formation, dated between 19 and 12 Ma (K–Ar ages on whole-rock and plagioclase from andesite) (Suárez and Emparan, 1997).

The northern termination of the LOFS consists of three fault sets (Fig. 3). (1) NNE-striking subvertical master faults (first order), (2) NE-striking, steeply-dipping splay faults (second order) and (3) ENE to EW-striking, steeply to moderately dipping local faults (third order).

Fig. 6. (a) Satellite image showing major faults (black lines), lineaments (dotted line), vein orientation (cyan line) and hot springs (blue symbol) at Las Mentas and La Poza structural sites. Las Mentas structural site: (b) strongly foliated (N05°W/81°W) rock deformed band (N20°E/70°W) crosscut by ENE-striking veins. (c) Oriented thin section from the deformed band consists of andesitic rock with preferentially oriented, undeformed plagioclase crystals forming sigmoidal S–C fabrics that indicate dextral displacement.

First-order faults are tens of km-long, which are represented by two subparallel faults: Malalcahuello and Troyo Faults as well as by four synthetic NNE-striking faults in the northern area (Fig. 4a). The Malalcahuello Fault is marked by a series of aligned scarps and valleys, mostly covered by Holocene volcanic rocks derived from the Llaima, Lonquimay, Tolhuaca and Callaqui volcanoes. A transfer zone is recorded by NE-trending alignment volcanic vents and fissure at the Lonquimay volcano. This transfer zone appears to connect the Malalcahuello fault with Lolco fault (Fig. 3). Lolco fault is a right-lateral strike slip fault, which splays off northward into two NE-striking faults forming one typical horsetail geometry (Fig. 3). At Lolco structural site (Fig. 4a) several cm-scale thick, right-lateral strike-slip faults exhibit zeolite slickenfibers (Fig. 4c). This fault zone cuts andesite and tuff belonging to the Cura–Mallin Fm. (12.0 ± 1.6, K–Ar) (supplemental figure SM1b). A synthetic fault zone is recorded at Ralco structural site (Fig. 4a). Here, faults and veins are mostly randomly oriented and locally parallel to shale (host rock) lamination. Locally, dilatational jogs are formed at linking zones between NNE- and NE-striking faults (Fig. 5a). Syntaxial bladed-like calcite crystals of about 1 cm in size fill these dilatational jogs (Fig. 5b). From outcrop to micro scales, NE-striking laumontite-, calcite-filled veins and hybrid faults relate both spatially and genetically to master faults (supplemental figures SM1b1 and c2). Fig. 5c shows a hybrid fault on a thin section from a N45°E/80°W oriented, right-lateral strike-slip fault. This section shows a calcite slickenfiber with several parallel sheets with sharp contact surfaces (Fig. 5d) and a transitional texture from a brittle shear zone in the host rock contact (Fig. 5d, b) to blocky crystals following the slip direction. The thin section also shows a couple of calcite extension veins (N70°E) genetically and kinematically related to master faults (Fig. 5b, a). Two synthetic NNE-faults are documented at Troyo structural site and vicinity (Fig. 4a). One is a right-lateral fault-slip with 10 cm thick of gouge fault core that crosscuts an EW-striking (Fig. 4b) fault and is spatially and kinematically related to NE-striking veins and hydrothermal breccia at Troyo structural site. The second fault, further east, is a dextral-reverse oblique fault-slip gently dipping (50°E) with 20 cm thick gouge core (supplemental figure SM1d). A rectilinear NS-striking valley is the morphological expression of Troyo Fault Zone. Along this valley, at Las Mentas structural site (Fig. 6a), NNE-striking master faults locally host a synkinematic strongly deformed andesitic dike (Fig. 5b). A thin section made in this deformed rock record a dextral slip documented by sigmoidal S–C fabrics (Fig. 5c). NE-striking veins (Fig 5c) crosscut this deformed band and NE-striking second order faults (Table 1).

Second order faults are NE-striking normal-dextral oblique slip and right lateral strike-slip faults that locally connect and cut some of the master and synthetic NNE-striking faults (e.g. Las Raices and La Poza

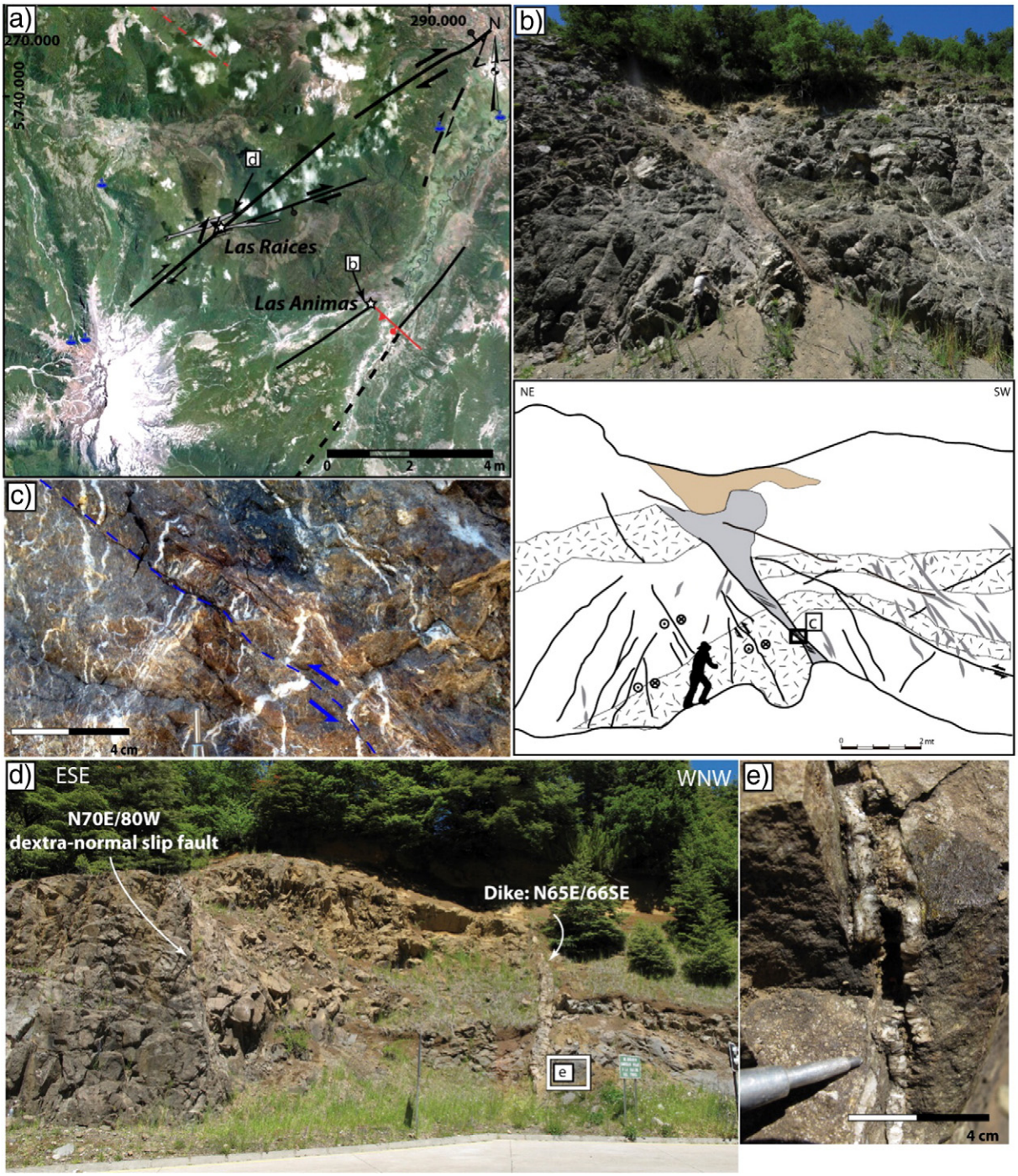

Fig. 7. (a) Google Earth image showing the major faults (black lines) and lineaments (dotted line) at the Las Raices and Las Animas structural sites. Las Animas structural site: (b) photograph and related line-drawing of one NW-striking fault showing a volcanic interlayered sequence of andesite and hornblende andesite forming a gentle anticline fold near the fault core, which corresponds to a fault-propagated fold. The fault core consists of a foliated gouge with Ca-rich zeolite veins cut by small reverse faults (c). Las Raices structural site: (d) photograph SSW view showing NE-striking normal-dextral slip fault and NE-striking dike cut by ENE-striking tensional zeolite veins (e).

structural site, Fig. 3). At regional scale, these fault-fracture networks host volcanic vents and dikes (Fig. 2, Fig 3). Las Raices structural site is a representative outcrop of second order faults (Fig. 7). Here, NE-striking dextral-normal oblique faults consist of 10 to 50 cm thick-banded fault core formed by laumontite and stilbite veins and hydrothermal breccia (supplemental figures SM2b, b1 and b2) (Las Raices structural site, Table 1). These crosscut NNE-striking dextral-reverse oblique slip faults with calcite slickenfibers. The NE-striking fault damage zone is rather asymmetric (Fig. 7d and supplemental figure SM2b), being more penetrative in the hanging wall than in the footwall. These fault-fracture networks host syntectonic N65°E-striking dikes (Fig. 7d) which are cut by N70°–80°E-striking, syntaxial, stilbite veins (Fig. 7e, supplemental figure SM2b and Table 1).

The third-order fault-fractures consist of cm-scale, sinistral-reverse faults locally exhibiting calcite slickenfibers and ENE- to WNW-striking veins and hydrothermal breccias. One of these vein systems is well recorded at outcrop scale at Las Mentas structural site. This consisting of one ENE–WNW/70°–45°S striking vein system filled with

euhedral calcite grains ranging between 0.3 and 2.0 cm in diameter. These hybrid faults and vein networks are commonly present at second order outcrop faults.

The Biobio–Alumine Fault System, despite being a well-marked lineament in the study area, record no obvious outcrops. Nevertheless, along stretches of the Biobío river valley, there are well-exposed decametric triangular facets and outcrop-scale normal faults developed on fluvial deposits indicating neotectonic activity. The master faults of the LOFS locally cut and displace those of the BAFS at regional scale (Fig. 3, 4a).

Numerous hot springs located at the NW flank of the Tolhuaca volcano also define a NW-trending alignment with hydrothermal alteration (Fig. 3). Las Animas structural site is a representative outcrop of NW-striking faults belonging to ATF (Fig. 7a). Here, a ca. 60 m wide, NW-striking fault zone is well exposed, consisting of two subparallel NW-striking faults with thickness of 30–50 m and two well-exposed 2–6 m thick faults with breccia and hydrothermal breccia fault cores (supplemental figures SM2c, c1 and c2).

One N50°W-striking fault (Fig. 7a, b) exhibits a foliated, 50 cm thick core with zeolite veins. These veins are cross-cut by cm-scale offset NW-striking reverse faults (Fig. 7c). Here, an asymmetrical hanging wall damage zone developed, showing a significant hydrothermal alteration expressed as a denser occurrence of sub-vertical stilbite filled veins and laumontite/stilbite rich matrix hydrothermal breccias (Fig. 7b) (Las Animas site, Table 1). A gentle, fault-propagated fold near the fault core confirms a reverse movement (Fig. 7b). The fault breccia consists of zeolite-filled vein-breccia that locally develops stockworks and lenticular, clast-supported zeolite hydrothermal breccia bodies with sub-rounded host-rock clasts ranging from 10 to 30 cm in diameter (supplemental figures SM2c, c1 and c2).

4.2. Kinematics and dynamics of fault-fracture networks

4.2.1. Regional fault slip analysis

Regional kinematic and dynamic parameters result from applying inversion procedures, seeking strain and stress fields representative of the entire fault population (n = 190) collected from 7 structural sites and vicinities (Fig. 8a). The regional strain analysis shows that individual (single fault datum) P and T axes are widely distributed, without forming well-defined clusters. This suggests that the analyzed fault-slip data population carries kinematically heterogeneous information about the faulting mechanism and evolution of the intra-arc zone. Following this, the strain analysis would not be representative without an arbitrary data selection (Angelier, 1984; Federico et al., 2010; Marrett and Allmendinger, 1990; Veloso et al., 2015; Yamaji, 2000). We analyze the fault-slip data by structural sites in an attempt to differentiate local-scale homogeneous strain fields recorded within the regionally heterogeneous fault-data set, as shown further along in the text.

Regional stress analysis shows a bimodal φ-histogram distribution with modes at 0.4–0.5 and at 0.9 (Fig. 8d). However, clustering of stress axes solutions have associated φ−values of 0.38 and 0.90. The transpressional strike-slip stress field associated with a φ-value of 0.38 yields a N64°E-trending subhorizontal σ_1 axis and a N30°W-trending subhorizontal σ_3 (Fig. 8c, e). The transtensional strike-slip field associated with a φ−value of 0.9 has an EW-trending subhorizontal σ_1 axis and NS-trending subhorizontal σ_3 (Fig 8c, e).

4.2.2. Local fault-slip analysis

A summary of the strain and stress field results of fault-slip data at each structural site is shown in Fig. 9 and in Table 1.

The NNE-striking fault zones show a homogeneous deformation with well-defined clusters of P- and T-axes (Lolco and Troyo structural sites). The principal strain axes solution indicate NW-trending stretching and NE-trending shortening with plane- to flattening-strain ellipsoid. At Ralco structural site, fault-slip data recorded the reactivation of shale lamination, showing a wide distribution of P- and T-axes. The stress axes solution shows a strike-slip tectonic regime (φ = ~0.50) with a subhorizontal NE-trending σ_1 and NW-trending σ_3 axes. The orientation of strain and stress axes solutions shows a good agreement for these NNE-striking set of faults.

The second order NE-trending faults, well represented at Las Raices structural site (Fig. 9 and Table 1); show a preferential clustering of T-axes on a NNW-trending direction and a wide distribution of P-axes with plane-strain ellipsoid. This kinematically heterogeneous faulting could be attributed to strain compatibility (Marrett and Allmendinger, 1990) between two fault sets, with slip parallel to fault intersection (Las Raices structural site, Fig. 9). The stress analysis indicates a transpressional regime (φ = 0.20) with an ENE-trending σ_1 and a subhorizontal NNW-trending σ_3. The minimum principal stress axis, σ_3, changes plunge to nearly sub-vertical (compressional tectonic regime) at the intersection with the LOFS master faults (La Poza structural site, Fig. 9).

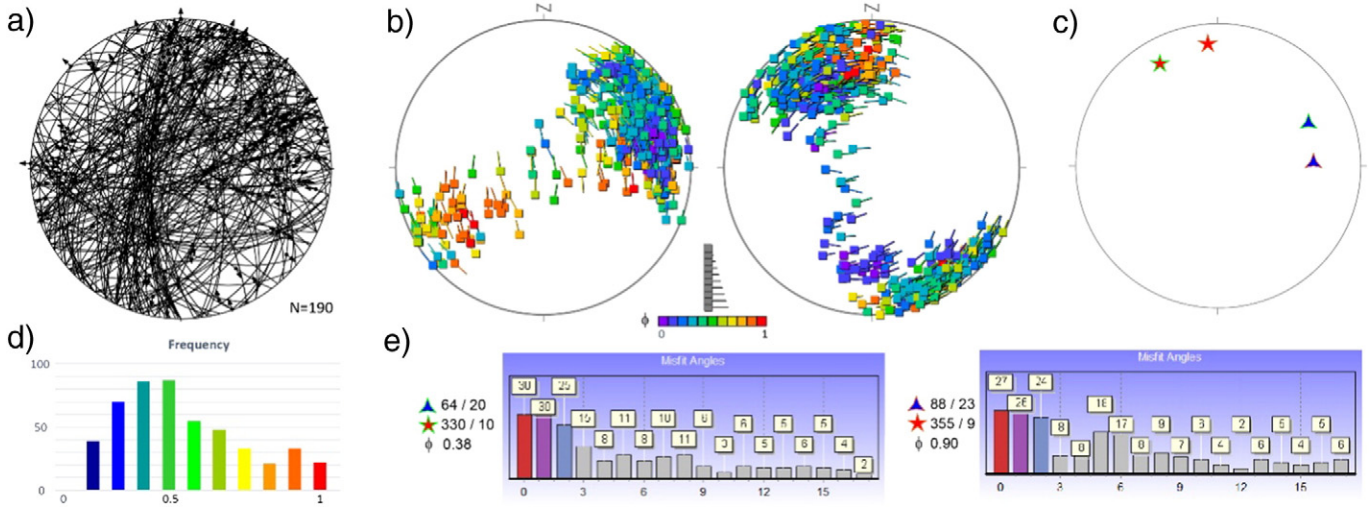

Fig. 8. (a) Lower hemisphere, equal-area projection showing the orientation of measured fault planes and their associated displacement vector (striae); (b) stress field solutions as given by the MIM method applied to our study area. Results of these analyses show the lower hemisphere stereonet (σ_1 and σ_3 to the left and right side, respectively, Fig. 7b)) calculated by using Multiple Inverse Method (MIM) (Yamaji, 2000), the color represents the φ-value from purple to red (0–1, respectively). (b) φ-histogram graph shows a bi-modal distribution of the best-possible fit between real and modeled data. (c) Stress field solutions from MIM, σ_1 (blue triangle) and σ_3 (red star) with red and green lines for φ = 0.9 and 0.38 respectively. (d) Graph showing the angular misfit for each solution.

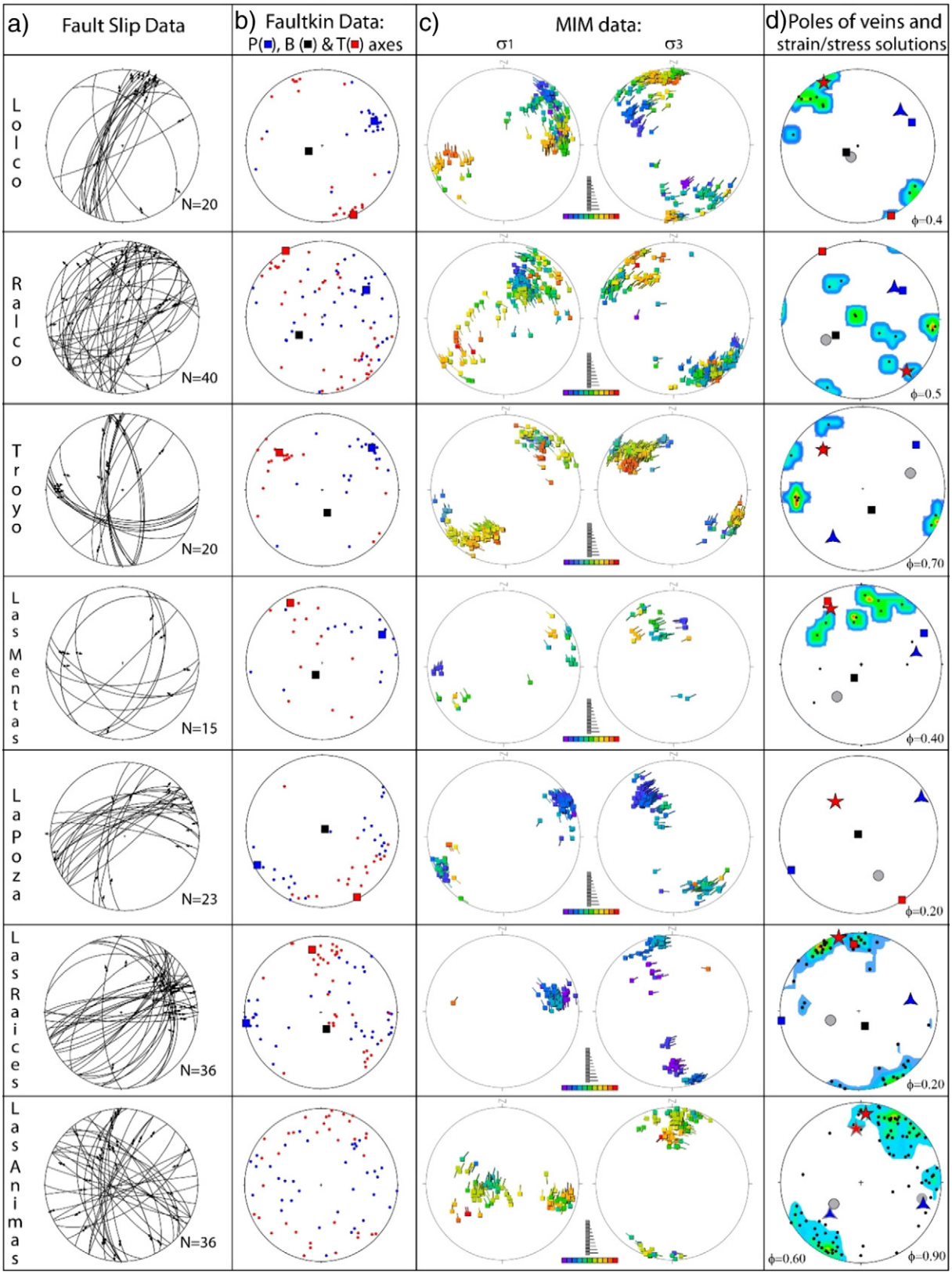

Fig. 9. Lower hemisphere, equal-area projections showing gathered fault-slip data and results of strain and stress analyses, at each structural site. (a) Mesoscopic fault-slip data; (b) orientation of T (red dots), P (blue dots) and B (black) axes (e.g. Marrett and Allmendinger, 1990). (c) Orientation of calculated stress axes (σ_1 and σ_3) MIM (Yamaji, 2000). (d) Density diagram of the poles-to-veins together with the orientation of σ_1 (triangle), σ_2 (circle) and σ_3 (star) principal stress axes shown in (c).

Fault-slip data analysis from Las Animas structural site shows a widely scattered distribution of both P- and T-axes, suggesting a polyphasic deformation and/or a pre-existing anisotropy reactivation. Similarly, dynamic analysis of the same ATF data with the aid of the MIM shows two distinctive stress axes solutions. The obtained strike-slip and tensional local stress fields share a common subhorizontal, N-trending σ_3 axes, but the minimum and intermediate stresses switch position, defining one strong solution with a subhorizontal, ESE-trending σ_1 in a strike-slip regime ($\varphi = 0.6$), and a secondary solution with a moderately plunging, WSW-trending σ_1 in a transtensional regime ($\varphi = 0.9$).

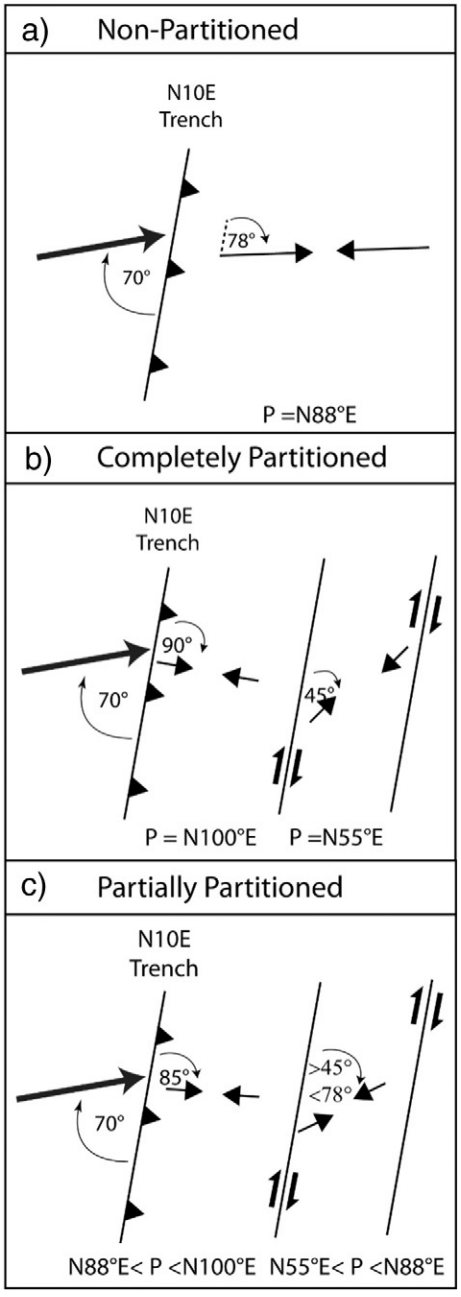

Fig. 10. Transpressional strain partitioned model (e.g Fossen et al., 1994; Teyssier et al., 1995) applied to the study area (a) non-partitioned, (b) completely partitioned and (c) partially partitioned strain; showing shortening-trending axis (P).

5. Discussion

5.1. Deformation partitioning at the Southern Volcanic Zone

Deformation partitioning arising from oblique convergence can be analyzed by using a geometrical relationship between the angle of relative plate motion and the trench (convergence angle $\alpha = 70°$; Fig. 10) and the orientation of maximum strain axes in the forearc and intra-arc domains (Teyssier et al., 1995). This geometrical analysis uses the kinematic model of strike-slip partitioning developed by Teyssier et al. (1995). This model is based on two end-members: strike-slip non-partitioned and completely partitioned. Based in this model, the non-partitioned deformation indicates a fixed orientation of the maximum shortening axis (i.e. P-axis) of N88°E, which is evenly distributed throughout the forearc and intra-arc domains (Fig. 10a). Conversely, in the case of a completely partitioned transpression, P-axis ought to trend N100°E in the forearc and N55°E in the intra-arc structural domain of the LOFS (Fig. 10b). Based on these two end-members and the kinematic/dynamic analyses shown before, we postulate a partial strain partitioning for our study area (Fig. 10c) with P-axes preferentially oriented N88°–100°E in the forearc domain and N55°–88°E in the intra-arc domain. The strain and stress field results, from fault slip data in the intra-arc domain, provide the tectonic context to compare the nature of strike-slip partitioning with the geometrical model depicted on Fig. 10. As a first approximation, the orientation of the regional-scale strain axes is given by the average orientation of T- and P-axes obtained for the entire fault-slip data population (Fig. 8). Although our results show a good agreement with field observations at a local scale, the dispersion of both P- and T-axes obtained for the entire fault-slip data at the LOFS (intra-arc) domain is very high, preventing the calculation of a geologically representative average value. Another possibility is to use the stress field as a proxy for the infinitesimal strain. Thus, the orientation of the σ_1-axis would be parallel to that of the minimum horizontal strain axis (S_3 or P) of the incremental strain ellipsoid. This implicitly assumes that the orientation of both stress and incremental strain axes has remained coaxial through the faults history – i.e. since at least from the Late Miocene – in our study area.

The N64°E orientation of the maximum principal stress axis (σ_1) obtained for the intra-arc is consistent with a partially partitioned deformation (Fig. 10c). In this case, the maximum shortening direction within the forearc is likely to lie close to an EW-trend (N88°E < P < N100°E-N100°E). This orientation is favorable for the development (or reactivation) of NW-striking discontinuities as, most probably, sinistral-reverse faults. Such geometry and kinematics are compatible with seismic activity (Fig. 1b) and the kinematics proposed at a regional-scale (Glodny et al., 2008; Melnick et al., 2009) for the Mesozoic to recent history of the NW-striking Lanalhue Fault (Fig. 1; 11), a fault of the ATF running through both the intra-arc and the forearc region.

The stress axes orientation and stress ratio ($\varphi = 0.20$) obtained from the entire fault-slip data (Fig. 8) indicates that the intra-arc is dominated by strike-slip transpression compatible with plane to flattening strain at each structural site. Moreover, our results from the dynamic and kinematics analysis indicate that deformation is even further partitioned within the intra-arc itself. The main evidence for this is the difference between the local stress fields calculated at each structural site and the regional stress field calculated for the entire intra-arc zone. Fig. 11 shows the regional and local stress fields and the main structural elements identified within the intra-arc, presenting different scales of deformation. Within the intra-arc, there are NNE-striking faults recording right lateral strike-slip and other oblique-reverse right lateral strike-slip (Fig. 11). This is an evidence that intra-arc domain is accommodating pure and simple shear deformation. The principal stress axes for the second order faults are slightly oblique with respect to the regional stress field and show plunge variations at structural sites where fault intersections are present (La Poza structural site, Fig. 11, Table 1). Similarly, variation of local stress axes orientation within a fault systems

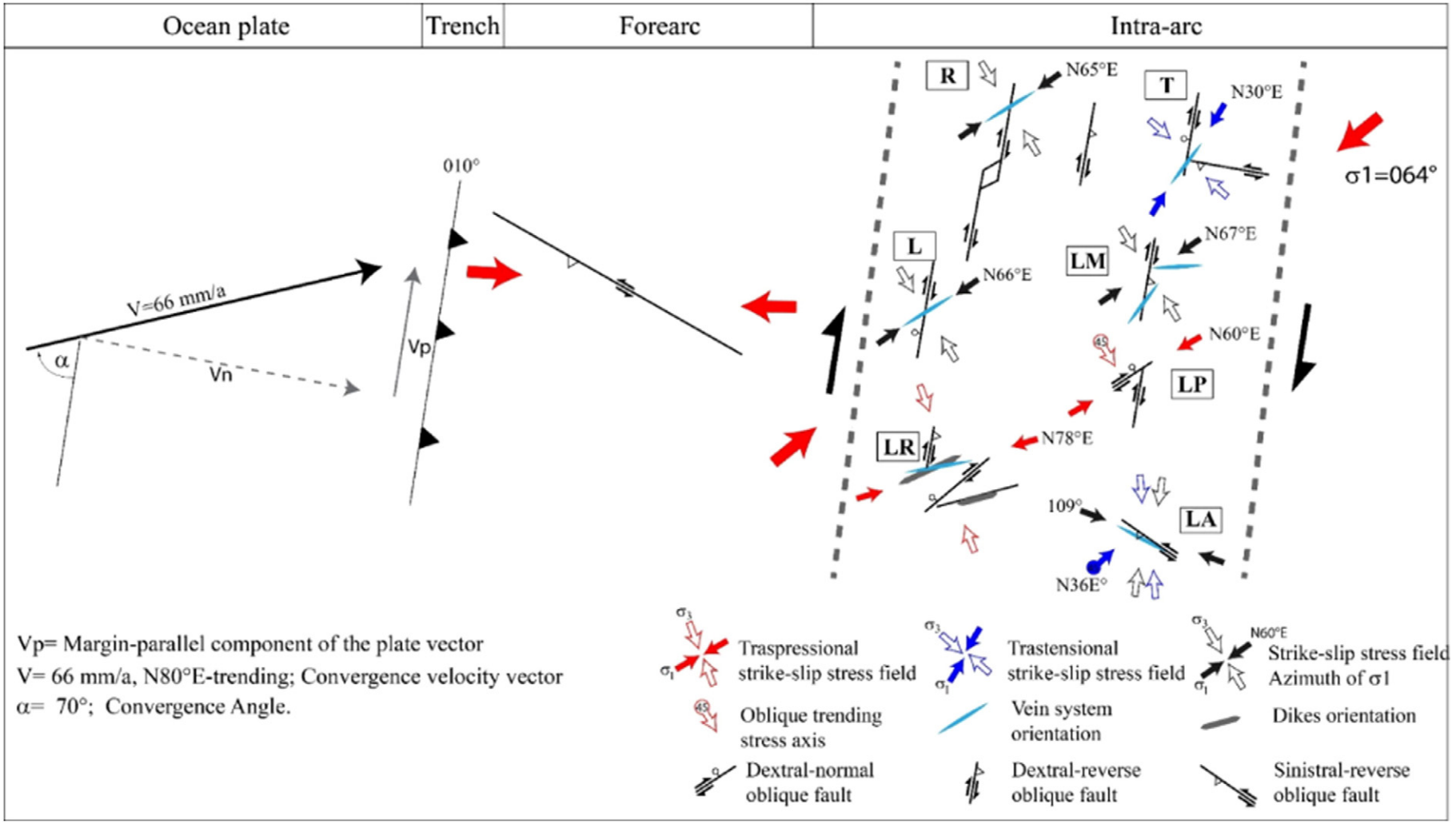

Fig. 11. Schematic diagram showing oblique convergence at 38°S and the strain partitioning analysis with the orientation of maximum shortening axes proposed for the forearc, and σ_1 direction calculated for the intra-arc region and the local stress field calculated for each structural site (R: Ralco, L: Lolco, T: Troyo, LP: La Poza, LM: Las Mentas, LR: Las Raices, LA: Las Animas). Details in Table 1.

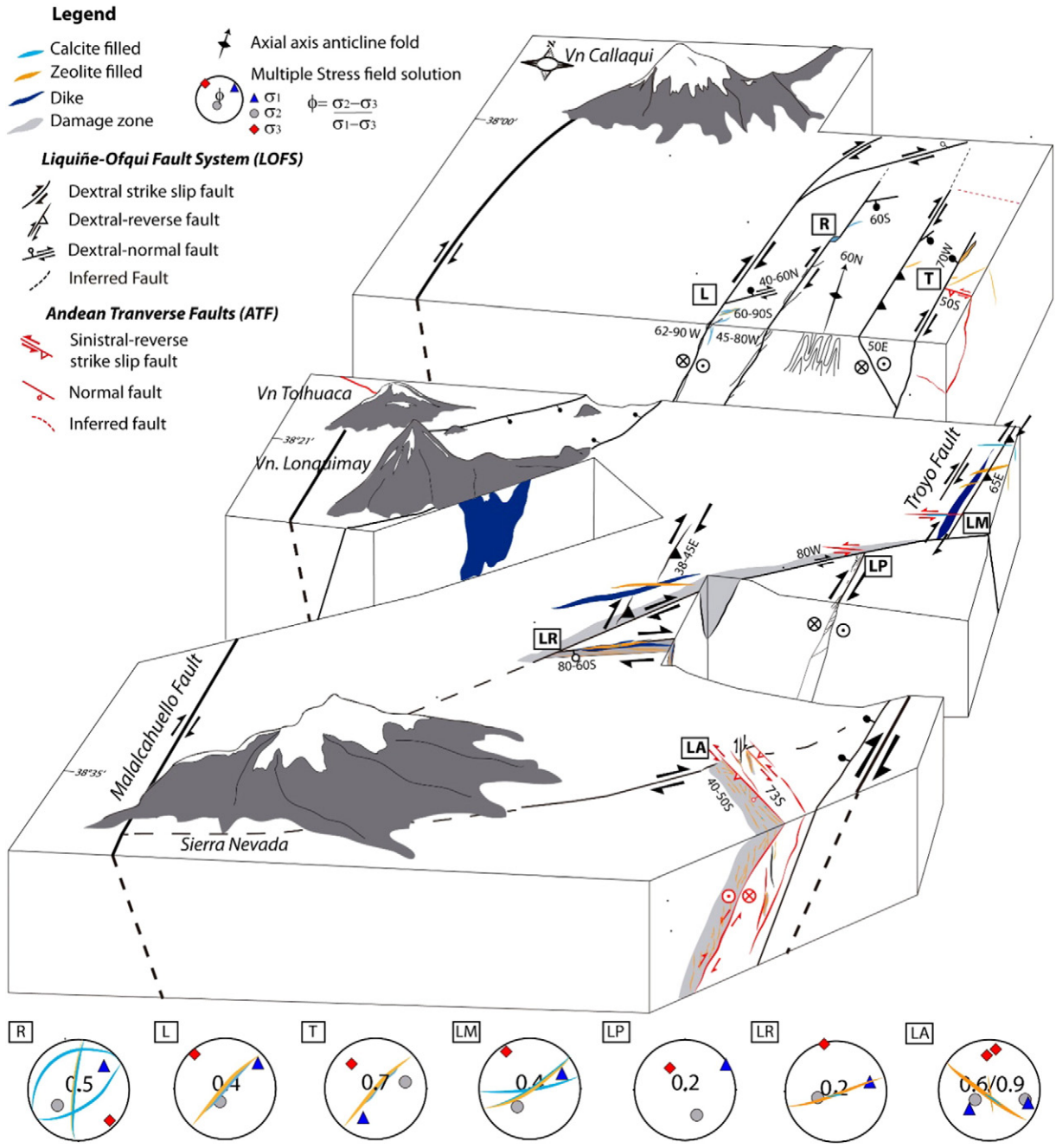

Fig. 12. Schematic block diagram illustrating the geometrical arrangement and kinematics of faults and other structural elements at the northern termination of the LOFS (black lines) together with the main traces of the ATF (red lines). The cartoon shows the local stress field solutions and the veins main orientation at each structural site (R: Ralco, L: Lolco, T: Troyo, LP: La Poza, LM: Las Mentas, LR: Las Raices, LA: Las Animas).

recorded by fault-slip data or earthquake focal mechanism has been documented at the Atacama Fault System (Veloso et al., 2015), South Island, New Zealand (Herman et al., 2014), Alhama de Murcia fault (Martínez-Díaz, 2002) and Maghreb region (Ousadou et al., 2014) among others.

Fault-slip data analysis of the LOFS structural elements yielded homogeneous orientations of the strain axes, suggesting that deformation occurred as a continuous deformation phase. In contrast, fault-slip data analysis of the ATF yielded heterogeneous orientations of the strain axes, suggesting that at least two deformation phases acted upon these structural elements. Accordingly, the MIM analysis shows two stress field solutions: one strike-slip ($\varphi = 0.6$) and one transtensional tectonic regime ($\varphi = 0.9$) (Figs. 11 and 12). Field observations at Las Animas structural site (Fig. 7b and c) document both stress field solutions, where one conspicuous NW-striking fault shows evidence of both normal-slip offset and of sinistral-reverse slip. The strike-slip local stress field solution ($\varphi = 0.6$) had a similar orientation to that of the theoretical maximum shortening axis previously discussed for fore-arc deformation (Fig. 11). These results record a deformation partitioning pattern within the intra-arc, accommodating part of the shortening perpendicular to the trench by sinistral-reverse NW-striking faults (Fig. 7c). The orientation of a second transtensional strike-slip stress field solution ($\varphi = 0.90$) is decoupled from the regional stress field and is consistent with the observed normal faulting and vertical veins networks present at the outcrop scale. This deformation pattern is similar to that obtained from focal mechanism analysis of the NW-striking Pichilemu fault during its reactivation after the Maule earthquake in the forearc domain (Aron et al., 2014, 2013).

Furthermore, a similar maximum stretching axis orientation of this solution was modeled for the co-seismic deformation during the 1960 Valdivia earthquake (Moreno et al., 2009; Plafker and Savage, 1970).

The geometry formed by right-lateral strike-slip NNE-striking master fault and dextral-reverse synthetic faults with NE-striking normal-dextral and NW-striking sinistral-reverse faults is compatible with the geometry shown in strike-slip analog model ($\sigma_1 = 45°$) (González et al., 2012). Nevertheless, this model records a fault system mainly composed of reverse-dextral faults accommodating the shortening imposed by oblique subduction. Our fault-slip data shows a strike-slip dominated fault system probably because the analog model does not include the subduction zone and forearc region, which accommodate most of the shortening component. Another important factor to consider is the thermal weakness present at the intra-arc region, not considered in the analog model.

5.2. Magmatic and hydrothermal fluid migration

The integration of strain and stress analysis of fault-fracture networks with the microstructural analyses of minerals from different structural elements allows constraining the tectonic and mechanical conditions operating during migration and crystallization of hydrothermal fluids and magmas (e.g. Bons et al., 2012). The transpressional strike-slip regime recorded in the intra-arc domain favors vertical magma/hydrothermal fluid migration (e.g. Brogi, 2011; Faulkner and Armitage, 2013; Sibson, 1994). The orientation of the regional stress field (N60E-striking σ_1 and N30W-striking σ_3 axes) seems to control the NE-striking orientation of volcanic feeder dikes observed at, for example, the Lonquimay, Llaima and Callaqui volcanoes. This is also recorded by the NE-elongation of stratovolcanoes and flanks vents NE-tending alignment (Fig. 2).

The NNE-to-NS-striking master faults of the LOFS record a strike-slip tectonic regime with similar orientation to that of the regional stress field. The NE-striking veins of this system are parallel to the orientation of σ_1 and perpendicular to σ_3 (Fig. 12). This fault-vein network reveals multiple reactivation events and coeval mineral precipitation at centimeter-scale (slickenfibers). Dilational jogs, which are likely to serve as efficient fluid conduits, are preferentially located at the intersection between NNE- and NE-striking faults (Fig. 12, Lolco and Ralco). Bladed-like texture of calcite aggregates sealing those dilational jogs suggests that fault activity triggered mineral precipitation by transient changes in the pore fluid pressure (Sibson, 1987; Weatherley and Henley, 2013).

The second order faults of the LOFS are spatially and genetically associated with ENE-striking veins compatible with the orientation of the calculated local stress field (Figs. 11 and 12 Las Raices structural site). Dikes preferentially intrude NE-striking decametric faults, which are reused by ENE-NE-striking tensional veins filled with zeolite and hydrothermal breccia lenses. Magma intrusion and superimposed hydrothermal activity record the favorable orientation of NE-ENE-striking faults and fractures to vertical magma/fluid transport at different times and depths. The third order structures of the LOFS are mainly represented by EW-striking tensional veins filled with zeolite and calcite, hybrid veins and hydrothermal breccias at the outcrop scale, which are compatible with the local stress field produced by second order faults (Figs. 11, 12, Las Mentas).

The ATF faults are composed of a thick damage zone and multiple fault cores and host thicker and more pervasive NW-striking veins and breccia bodies than the LOFS (Table 1; Figs. 11, 12, Las Animas structural site). Despite the fact that these NW-striking faults are kinematically compatible with the stress field, they have an unfavorable orientation for faulting and therefore, are likely to require high fluid-pore pressure to rupture (e.g. Sibson, 2004). Overpressure conditions are likely to form breccia bodies and stockworks at meter-scale and to produce large pore fluid pressure fluctuations. Therefore, structural elements related to the ATF faults are not only suitable for magma and/or hydrothermal migration but also for transient fluid storage.

Minerals precipitated within fault-fractures network are mainly zeolite (stilbite and laumontite) and locally calcite. The hydrothermal activity temperature recorded by laumontite + stilbite assemblage indicates crystallization temperatures at 110–170 °C (Liou et al., 1987). The different minerals do not reveal, at regional scale, a preferential distribution or a clear spatial association with a particular structural element. Evidence recorded at the NW-striking discontinuities reflects the higher volume of mineral precipitation and associated larger damage zone. Similar mineralogy has been recognized at shallow depths (≤500 m) in active hydrothermal systems from the Southern Andes Volcanic Zone, such as Tolhuaca and Copahue Geothermal Fields (Mas et al., 2005; Mas, 2005; Melosh et al., 2012, 2010). These active systems are also spatially related to both the LOFS and the ATF faults, suggesting that they might be the present-day active analogs of the structural sites analyzed.

Thus, our results show the complexity in the spatial distribution of stress fields within strike-slip systems and their role in the geometrical distribution of fluid flow, part of which may account for the reactivation of inherited faults or strain incompatibilities at fault intersections. Our work suggests that the structural elements, and the systems that they define, record a long-lived deformation coeval with magma/fluid migration within the crust, from early magmatic stages to late hydrothermal mineral precipitation (veins) that used, essentially, the same discontinuities over time and space.

6. Conclusions

A complete analysis of structural elements at the intra-arc domain of the LOFS and ATF between 38°S and 39°S reveals the mechanism of control that the regional and local stress fields exert on magma/fluid transport and arrest (Fig. 12). Our conclusions are summarized as follows:

1- Deformation driven by oblique convergence is partially partitioned into each morphotectonic domain: subduction zone, forearc and intra-arc. At intra-arc domain, the tectonic regime corresponds to a strike-slip-dominated transpression (Fig. 11).
2- The regional stress field at the intra-arc region is the result of two independent and homogeneous stress fields. The prevailing stress field solution corresponds to a transpressional stress regime with a subhorizontal, N64°E-trending σ_1 axis and a subhorizontal, N30°W-trending, σ_3 axis. The second identified stress field solution is a transtensional stress regime with a subhorizontal, N88°E-trending σ_1 axis and a subhorizontal N05°W-trending σ_3 axis.
3- Deformation is also further partitioned within the intra-arc domain by faults with NNE-, NE-, ENE- and NW-strikes. Particular features of these faults are:
   a. The NNE-striking faults show either right lateral strike-slip and dextral-reverse displacement, accommodating part of the trench-parallel and trench-orthogonal shortening components.
   b. The NE-striking faults are mostly hybrid faults with dextral-normal displacements. The associated transpressional local stress regime is clockwise-rotated with respect to the regional solution, thus favoring the emplacement of ENE-striking veins and dikes. At the intersection between NE- and NNE-striking faults, the stress regime is nearly compressive.
   c. The NW-striking faults document two different kinematic and dynamic behaviors. One of them is compatible with the regional stress field and accommodates the orthogonal to the trench-shortening component. The second stress field solution is decoupled from the prevailing regional stress field and has a stronger long-term deformation imprint at the outcrop scale.
4- The LOFS constitutes a localized fluid/magma pathway, where NNE-striking master faults focus the emplacement of syntectonic dike

intrusions and the distribution of arrested paleo-fluids mainly at dilational jogs. The NE-striking fault-fractures host dikes and volcanic vents at kilometric scale, according with tensional fractures activated by the regional stress field. These structural elements constitute pathways for magma and hydrothermal fluid migration. The local stress field variation has a strong control on the vein systems and dikes orientation at outcrop scale.

5- ATF may constitute a large hydrothermal fluid reservoir with wide fault zones and a strongly developed fault-fracture network spatially associated with mineral precipitation.

6- Our observations support a strong interplay between stress field, fault-fracture orientation and magma/paleofluid distribution. The fault-fracture networks favorably oriented for reactivation with respect to the regional stress field constitute well-defined vertical pathways for magma/fluid transport through the lithosphere. These structures define restricted damage zones and thin veins systems. Conversely, fault-fracture systems misoriented with respect to the regional stress field might act as efficient reservoir for magma and fluid under high fluid pressures.

Acknowledgments

We are grateful to Julie Rowland, Diego Morata, Martin Reich and Gerd Sielfeld for fruitful discussions on the interplay among tectonics, volcanism and hydrothermal fluid flow over the last years. Special thanks to the generous help of Martin Lizama during and after fieldwork, and to Felipe Astudillo and Juan Ignacio Sanchez who also helped in the fieldwork. We sincerely thank Associated Editor Rob Govers and reviewers Elena Druguet and Ozgur Karaoglu for their constructive comments on the manuscript. We also thank Tom Mitchell for hosting PPF at the UCL Rock Preparation Laboratory and Jim Davy for his help with thin sections preparation and SEM analysis. Thanks are also due to our colleagues Daniele Tardani, Rodrigo Gomila, Pablo Iturrieta, Ashley Stanton-Yonge and Felipe Aron; all of them shared their enthusiasm and ideas with us. This paper is a contribution to the Andean Geothermal Center of Excellence (CEGA) FONDAP/CONICYT Project 15090013 and FONDECYT Projects 1130030 (GA) and 1141139 (JC). Perez-Flores's PhD studies are funded by CONICYT — Beca Doctorado Nacional 21120519. Sanchez, P acknowledges support given by Millennium Science Initiative grant NC130065.

Appendix A. Supplementary data

Supplementary data to this article can be found online at http://dx.doi.org/10.1016/j.tecto.2016.05.016.

References

Acocella, V., Funiciello, R., 2006. Transverse systems along the extensional Tyrrhenian margin of central Italy and their influence on volcanism. Tectonics 25. http://dx.doi.org/10.1029/2005TC001845.

Allmendinger, R.W., Cardozo, N.C., Fisher, D., 2012. Structural Geology Algorithms: Vectors & Tensors. Cambridge University Press, Cambridge, England.

Angelier, J., 1984. Tectonic analysis of fault slip data sets. J. Geophys. Res. 89, 5835–5848.

Angermann, D., Klotz, J., Reigber, C., 1999. Space-geodetic estimation of the Nazca–South America Euler vector. Earth Planet. Sci. Lett. 171, 329–334. http://dx.doi.org/10.1016/S0012-821X(99)00173-9.

Arancibia, G., Cembrano, J., Lavenu, A., 1999. Transpresión dextral y partición de la deformación en la Zona de Falla Liquiñe–Ofqui, Aisén, Chile (44–45°S). Rev. Geol. Chile 26. http://dx.doi.org/10.4067/S0716-02081999000100001.

Aron, F., Allmendinger, R.W., Cembrano, J., González, G., Yáñez, G., 2013. Permanent forearc extension and seismic segmentation: insights from the 2010 Maule earthquake, Chile. J. Geophys. Res. Solid Earth 118, 724–739. http://dx.doi.org/10.1029/2012JB009339.

Aron, F., Cembrano, J., Astudillo, F., Allmendinger, R.W., Arancibia, G., 2014. Constructing forearc architecture over megathrust seismic cycles: geological snapshots from the Maule earthquake region, Chile. Geol. Soc. Am. Bull. 127, 464–479. http://dx.doi.org/10.1130/B31125.1.

Barrientos, S.E., Acevedo-Aránguiz, P.S., 1992. Seismological aspects of the 1988–1989 Lonquimay (Chile) volcanic eruption. J. Volcanol. Geotherm. Res. 53, 73–87. http://dx.doi.org/10.1016/0377-0273(92)90075-O.

Beck, M.E., 1988. Analysis of late Jurassic–recent paleomagnetic data from active plate margins of South America. J. South Am. Earth Sci. 1, 39–52. http://dx.doi.org/10.1016/0895-9811(88)90014-4.

Bellier, O., Zoback, M.L., 1995. Recent state of stress change in the Walker Lane zone, western Basin and Range province, United States. Tectonics 14, 564–593. http://dx.doi.org/10.1029/94TC00596.

Bertin, D., 2010. El complejo volcanico lonquimay y la zona de falla liquiñe-ofqui: estudio estructural, morfometrico y gravimetrico. Universidad de Chile.

Blanquat, M.D.S., Tikoff, B., Teyssier, C., Vigneresse, J.L., 1998. Transpressional kinematics and magmatic arcs. Geol. Soc. Lond. Spec. Publ. 135, 327–340. http://dx.doi.org/10.1144/GSL.SP.1998.135.01.21.

Bons, P.D., Elburg, M.A., Gomez-Rivas, E., 2012. Review article: a review of the formation of tectonic veins and their microstructures. J. Struct. Geol. 43, 33–62. http://dx.doi.org/10.1016/j.jsg.2012.07.005.

Bouvet de Maisonneuve, C., Dungan, M.A., Bachmann, O., Burgisser, A., 2012. Insights into shallow magma storage and crystallization at Volcán Llaima (Andean Southern Volcanic Zone, Chile). J. Volcanol. Geotherm. Res. 211–212, 76–91. http://dx.doi.org/10.1016/j.jvolgeores.2011.09.010.

Brogi, A., 2011. Variation in fracture patterns in damage zones related to strike-slip faults interfering with pre-existing fractures in sandstone (Calcione area, southern Tuscany, Italy). J. Struct. Geol. 33, 644–661. http://dx.doi.org/10.1016/j.jsg.2010.12.008.

Caine, J.S., Evans, J.P., Forster, C.B., 1996. Fault zone architecture and permeability structure. Geology http://dx.doi.org/10.1130/0091-7613(1996)024<1025.

Cande, S.C., Leslie, R.B., 1986. Late Cenozoic tectonics of the Southern Chile Trench. J. Geophys. Res. 91, 471–496.

Cembrano, J., Herve, F., 1993. The Liquiñe–Ofqui Fault Zone: A Major Cenozoic Strike Slip Duplex in the Southern Andes. Second ISAG. Oxford, UK, pp. 175–178.

Cembrano, J., Lara, L., 2009. The link between volcanism and tectonics in the southern volcanic zone of the Chilean Andes: a review. Tectonophysics 471, 96–113. http://dx.doi.org/10.1016/j.tecto.2009.02.038.

Cembrano, J., Moreno, H., 1994. Geometria y naturaleza costrastante del volcanismo cuaternario entre los 38°y 46°S: Dominios compresionales y tensionales en un régimen transcurrente? Congr. Geológico Chil. 7.

Cembrano, J., Herve, F., Lavenu, A., 1996. The Liquifie Ofqui fault zone: a long-lived intra-arc fault system in southern Chile. Tectonophysics 256, 55–56.

Cembrano, J., Schermer, E., Lavenu, A., Sanhueza, A., 2000. Contrasting nature of deformation along an intra-arc shear zone, the Liquiñe–Ofqui fault zone, southern Chilean Andes. Tectonophysics 319, 129–149.

Chernicoff, C.J., Richards, J.P., Zappettini, E.O., 2002. Crustal lineament control on magmatism and mineralization in northwestern Argentina: geological, geophysical, and remote sensing evidence. Ore Geol. Rev. 21, 127–155.

Cifuentes, I.L., 1989. The 1960 Chilean earthquakes. J. Geophys. Res. 94 (B1), 665. http://dx.doi.org/10.1029/JB094iB01p00665.

Connolly, P., Cosgrove, J., 1999. Prediction of fracture-induced permeability and fluid flow in the crust using experimental stress data. AAPG Bull. 83, 757–777.

Corazzato, C., Tibaldi, A., 2006. Fracture Control on Type, Morphology and Distribution of Parasitic Volcanic Cones: An Example From Mt. Etna, Italy. http://dx.doi.org/10.1016/j.jvolgeores.2006.04.018.

Cox, S.F., 1999. Deformational controls on the dynamics of fluid flow in mesothermal gold systems. Geol. Soc. London Spec. Publ. 155, 123–140. http://dx.doi.org/10.1144/GSL.SP.1999.155.01.10.

Cox, S.F., 2010. The application of failure mode diagrams for exploring the roles of fluid pressure and stress states in controlling styles of fracture-controlled permeability enhancement in faults and shear zones. Geofluids 217–233 http://dx.doi.org/10.1111/j.1468-8123.2010.00281.x.

Curewitz, D., Karson, J.A., 1997. Structural settings of hydrothermal outflow: fracture permeability maintained by fault propagation and interaction. J. Volcanol. Geotherm. Res. 79, 149–168. http://dx.doi.org/10.1016/S0377-0273(97)00027-9.

Dewey, J.F., Holdsworth, R.E., Strachan, R.A., 1998. Transpression and transtension zones. Geol. Soc. Lond. Spec. Publ. 135, 1–14. http://dx.doi.org/10.1144/GSL.SP.1998.135.01.01.

Diraison, M., Cobbold, P.R., Gapais, D., Rossello, E.A., Le Corre, C., 2000. Cenozoic crustal thickening, wrenching and rifting in the foothills of the southernmost Andes. Tectonophysics 316, 91–119. http://dx.doi.org/10.1016/S0040-1951(99)00255-3.

Dziewonski, A.M., Ekström, G., Woodhouse, J.H., Zwart, G., 1990. Centroid-moment Tensor Solutions for January–March 1989 59. pp. 233–242.

Fagereng, Å., Remitti, F., Sibson, R.H., 2011. Tectonophysics Incrementally Developed Slicken Fibers — Geological Record of Repeating Low Stress-drop Seismic Events? 510 pp. 381–386. http://dx.doi.org/10.1016/j.tecto.2011.08.015

Faulkner, D.R., Armitage, P.J., 2013. The effect of tectonic environment on permeability development around faults and in the brittle crust. Earth Planet. Sci. Lett. 375, 71–77. http://dx.doi.org/10.1016/j.epsl.2013.05.006.

Faulkner, D.R., Jackson, C.A.L., Lunn, R.J., Schlische, R.W., Shipton, Z.K., Wibberley, C.A.J., Withjack, M.O., 2010. A review of recent developments concerning the structure, mechanics and fluid flow properties of fault zones. J. Struct. Geol. http://dx.doi.org/10.1016/j.jsg.2010.06.009 Elsevier Ltd.

Federico, L., Crispini, L., Capponi, G., 2010. Fault-slip analysis and transpressional tectonics: A study of Paleozoic structures in northern Victoria Land, Antarctica. J. Struct. Geol. 32, 667–684. http://dx.doi.org/10.1016/j.jsg.2010.04.001.

Fitch, T.J., 1972. Plate convergence, transcurrent fault, and internal deformation adjacent to Southeast Asia and the Western Pacific. J. Geophys. Res. 77, 4432–4460.

Fossen, H., Tikoff, B., 1998. Geological Society, London, Special Publications Extended Models of Transpression and Transtension, and Application to Tectonic Settings Email Alerting Service Permission Extended Models of Transpression and Transtension, and Application to Tectonics. pp. 15–33 http://dx.doi.org/10.1144/GSL.SP.1998.135.01.02.

Fossen, H., Tikoff, B., Teyssier, C., 1994. Strain modeling of transpressional and transtensional deformation. Nor. Geol. Tidsskr.
Glodny, J., Echtler, H., Collao, S., Ardiles, M., Burón, P., Figueroa, O., 2008. Differential Late Paleozoic active margin evolution in South-Central Chile (37°S–40°S) — the Lanalhue Fault Zone. J. S. Am. Earth Sci. 26, 397–411. http://dx.doi.org/10.1016/j.jsames.2008.06.001.
González, D., Pinto, L., Peña, M., Arriagada, C., 2012. 3D deformation in strike-slip systems: analogue modelling and numerical restoration. Andean Geol. 39, 295–316. http://dx.doi.org/10.5027/andgeoV39n2-a06.
Gudmundsson, A., Berg, S.S., Lyslo, K.B., Skurtveit, E., 2001. Fracture networks and fluid transport in active fault zones. J. Struct. Geol. 23, 343–353. http://dx.doi.org/10.1016/S0191-8141(00)00100-0.
Haberland, C., Rietbrock, A., Lange, D., Bataille, K., Hofmann, S., 2006. Interaction between forearc and oceanic plate at the south-central Chilean margin as seen in local seismic data. Geophys. Res. Lett. 33, 1–5. http://dx.doi.org/10.1029/2006GL028189.
Herman, M.W., Herrmann, R.B., Benz, H.M., Furlong, K.P., 2014. Using regional moment tensors to constrain the kinematics and stress evolution of the 2010–2013 Canterbury earthquake sequence, South Island, New Zealand. Tectonophysics 633, 1–15.
Jarrard, R.D., 1986. Terrane motion by strike-slip faulting of forearc slivers. Geology 14, 780–783. http://dx.doi.org/10.1130/0091-7613(1986)14<780:TMBSFO>2.0.CO.
Karaoğlu, Ö., 2014. Tectonic controls on the Yamanlar volcano and Yuntdağı volcanic region, western Turkey: implications for an incremental deformation. J. Volcanol. Geotherm. Res. 274, 16–33.
Kolb, J., Rogers, A., Meyer, F.M., Siemes, H., 2005. Dominant coaxial deformation of veins during the interseismic stage of the fault-valve cycle: microfabrics of laminated quartz veins of the Hutti gold mine, India. J. Struct. Geol. 27, 2043–2057. http://dx.doi.org/10.1016/j.jsg.2005.06.005.
Lange, D., Cembrano, J., Rietbrock, A., Haberland, C., Dahm, T., Bataille, K., 2008. First seismic record for intra-arc strike-slip tectonics along the Liquiñe–Ofqui fault zone at the obliquely convergent plate margin of the southern Andes. Tectonophysics 455, 14–24. http://dx.doi.org/10.1016/j.tecto.2008.04.014.
Lara, L., Naranjo, J., Moreno, H., 2004. Rhyodacitic fissure eruption in Southern Andes (Cordón Caulle; 40.5°S) after the 1960 (Mw:9.5) Chilean earthquake: a structural interpretation. J. Volcanol. Geotherm. Res. 138, 127–138. http://dx.doi.org/10.1016/j.jvolgeores.2004.06.009.
Lara, L., Lavenu, A., Cembrano, J., Rodriguez, C., 2006. Structural controls of volcanism in transversal chains: resheared faults and neotectonics in the Cordón Caulle–Puyehue area (40.5°S), Southern Andes. J. Volcanol. Geotherm. Res. 158, 70–86. http://dx.doi.org/10.1016/j.jvolgeores.2006.04.017.
Lara, L.E., Cembrano, J., Lavenu, A., 2008. Quaternary vertical displacement along the Liquiñe–Ofqui Fault Zone: differential uplift and coeval volcanism in the Southern Andes? Int. Geol. Rev. 50, 975–993. http://dx.doi.org/10.2747/0020-6814.50.11.975.
Lavenu, A., Cembrano, J., 1999. Compressional- and transpressional-stress pattern for Pliocene and Quaternary brittle deformation in fore arc and intra-arc zones (Andes of Central and Southern Chile). J. Struct. Geol. 21, 1669–1691. http://dx.doi.org/10.1016/S0191-8141(99)00111-X.
Legrand, D., Barrientos, S., Bataille, K., Cembrano, J., Pavez, A., 2011. The fluid-driven tectonic swarm of Aysen Fjord, Chile (2007) associated with two earthquakes (Mw = 6.1 and Mw = 6.2) within the Liquiñe–Ofqui Fault Zone. Cont. Shelf Res. 31, 154–161. http://dx.doi.org/10.1016/j.csr.2010.05.008.
Lin, Y.N., Sladen, A., Ortega-Culaciati, F., Simons, M., Avouac, J., Fielding, E.J., Socquet, A., 2013. Coseismic and postseismic slip associated with the 2010 Maule Earthquake, Chile: Characterizing the Arauco Peninsula barrier effect. 118, 3142–3159. http://dx.doi.org/10.1002/jgrb.50207.
Liou, J.G., Maruyama, S., Cho, M., 1987. Very Low-grade Metamorphism of Volcanic and Volcaniclastic Rocks: Mineral Assemblages and Mineral Facies. In: Frey, M. (Ed.), Very Low-grade Metamorphism. Blackie, Glasgow and London, Glasgow and London.
López-Escobar, L., Cembrano, J., Moreno, H., 1995. Geochemistry and tectonics of the Chilean Southern Andes basaltic Quaternary volcanism. Andean Geol. 22, 219–234.
Marrett, R., Allmendinger, R.W., 1990. Kinematic analysis of fault-slip data. J. Struct. Geol. 12, 973–986.
Martínez-Díaz, J.J., 2002. Stress field variation related to fault interaction in a reverse oblique-slip fault: the Alhama de Murcia fault, Betic Cordillera, Spain. Tectonophysics 356, 291–305.
Mas, L.C., 2005. Present Status of the Copahue Geothermal Project. World Geothermal Congress. Antalya, Turkey, Turkey.
Mas, G.R., Bengochea, L., Mas, L.C., 2005. Thermometric Study of Copahue Geothermal Field; Argentina. World Geothermal Congress 2005. Antalya, Turkey, Turkey.
Maurice, J., 2012. Geochemical and Structural Constraints on Magma Storage at Llaima Volcano. A Support for Shallow Dikes Reservoirs. Graduate School of State University of New York.
Mccaffrey, K.J.W., 1992. Igneous Emplacement in a Transpressive Shear Zone. Ox Mountains igneous complex. 149, pp. 221–235.
Melnick, D., Folguera, A., Ramos, V., 2006a. Structural control on arc volcanism: the Caviahue–Copahue complex, Central to Patagonian Andes transition (38°S). J. S. Am. Earth Sci. 22, 66–88. http://dx.doi.org/10.1016/j.jsames.2006.08.008.
Melnick, D., Rosenau, M., Folguera, A., Echtler, H., 2006b. Neogene tectonic evolution of the Neuquén Andes western flank (37–39°S). Geol. Soc. Spec. Pap. 407.
Melnick, D., Bookhagen, B., Strecker, M.R., Echtler, H.P., 2009. Segmentation of megathrust rupture zones from forearc deformation patterns over hundreds to millions of years, Arauco peninsula, Chile. J. Geophys. Res. 114, B01407. http://dx.doi.org/10.1029/2008JB005788.
Melosh, G., Cumming, W., Benoit, D., Wilmarth, M., Colvin, A., Winick, J., Soto-, E., Sussman, D., Urzúa-monsalve, L., Powell, T., Peretz, A., 2010. Exploration Results and Resource Conceptual Model of the Tolhuaca Gethermal Field, Chile. Proceedings World Geothermal Congress. Bali, Indonesia, pp. 25–29.
Melosh, G., Moore, J., Stacey, R., 2012. Natural Reservoir Evolution in the Tolhuaca Geothermal Field, Southern Chile. Thirty-sixth Workshop on Geothermal Reservoir Engineering. Stanford, California, United States, California, United States.
Melosh, B.L., Rowe, C.D., Smit, L., Groenewald, C., Lambert, C.W., Macey, P., 2014. Snap, Crackle. Pop: Dilational Fault Breccias Record Seismic Slip Below the Brittle–Plastic Transition. 403, pp. 432–445.
Micklethwaite, S., Cox, S.F., 2004. Fault-segment rupture, aftershock-zone fluid flow, and mineralization. Geology 32, 813. http://dx.doi.org/10.1130/G20559.1.
Mitchell, T.M., Faulkner, D.R., 2012. Towards quantifying the matrix permeability of fault damage zones in low porosity rocks. Earth Planet. Sci. Lett. 339–340, 24–31. http://dx.doi.org/10.1016/j.epsl.2012.05.014.
Moeck, I., Kwiatek, G., Zimmermann, G., 2009. Slip tendency analysis, fault reactivation potential and induced seismicity in a deep geothermal reservoir. J. Struct. Geol. 31, 1174–1182. http://dx.doi.org/10.1016/j.jsg.2009.06.012.
Moncada, D., Mutchler, S., Nieto, A., Reynolds, T.J., Rimstidt, J.D., Bodnar, R.J., 2012. Mineral textures and fluid inclusion petrography of the epithermal Ag–Au deposits at Guanajuato, Mexico: Application to exploration. J. Geochemical Explor. 114, 20–35. http://dx.doi.org/10.1016/j.gexplo.2011.12.001.
Moreno, M.S., Bolte, J., Klotz, J., Melnick, D., 2009. Impact of megathrust geometry on inversion of coseismic slip from geodetic data: application to the 1960 Chile earthquake. Geophys. Res. Lett. 36, 1–5. http://dx.doi.org/10.1029/2009GL039276.
Muñoz, J., Stern, C.R.R., 1988. The quaternary volcanic belt of the southern continental margin of South America: transverse structural and petrochemical variations across the segment between 38°S and 39°S. J. S. Am. Earth Sci. 1, 147–161. http://dx.doi.org/10.1016/0895-9811(88)90032-6.
Nakamura, K., 1977. Volcanoes as possible indicators of tectonic stress orientation — principle and proposal. J. Volcanol. Geotherm. Res. 2, 1–16. http://dx.doi.org/10.1007/BF01637099.
Otsubo, M., Sato, K., Yamaji, A., 2006. Computerized identification of stress tensors determined from heterogeneous fault-slip data by combining the multiple inverse method and k-means clustering. J. Struct. Geol. 28, 991–997. http://dx.doi.org/10.1016/j.jsg.2006.03.008.
Ousadou, F., Dorbath, L., Ayadi, A., Dorbath, C., 2014. Stress field variations along the Maghreb region derived from inversion of major seismic crisis fault plane solutions. Tectonophysics 632, 261–280.
Pardo-Casas, F., Molnar, P., 1987. Relative Motion of the Nazca (Farellon) and South American Plates Since Late Cretaceous Time. 6 pp. 233–248.
Plafker, G., Savage, J.C., 1970. Mechanism of the Chilean Earthquakes of May 21 and 22, 1960. Geol. Soc. Am. Bull. 81, 1001–1030.
Power, W.L., Tullis, T.E., 1989. The relationship between slickenside surfaces in fine-grained quartz and the seismic cycle. J. Struct. Geol. 11, 879–893. http://dx.doi.org/10.1016/0191-8141(89)90105-3.
Radic, J.P., 2010. Las cuencas cenozoicas y su control en el volcanismo de los Complejos Nevados de Chillán y Copahue–Callaqui (Andes del Sur, 36–39 ° S). Andean Geol. 37, 220–246.
Ritz, J.-F., 1994. Determining the slip vector by graphical construction: use of a simplified representation of the stress tensor. J. Struct. Geol. 16, 737–741.
Rosenau, M., Melnick, D., Echtler, H., 2006. Kinematic constraints on intra-arc shear and strain partitioning in the southern Andes between 38 ° S and 42 ° S latitude. Tectonics 25, 1–16. http://dx.doi.org/10.1029/2005TC001943.
Rowland, J.V., Sibson, R.H., 2004. Structural controls on hydrothermal flow in a segmented rift system, Taupo Volcanic Zone, New Zealand. Geofluids 4, 259–283. http://dx.doi.org/10.1111/j.1468-8123.2004.00091.x.
Sánchez, P., Pérez-Flores, P., Reich, M., Arancibia, G., Cembrano, J., Taylor, P., Sánchez, P., Reich, M., Pérez-flores, P., Arancibia, G., 2013. Crustal deformation effects on the chemical evolution of geothermal systems: the intra-arc Liquiñe–Ofqui Fault System, Southern Andes. Int. Geol. Rev. 37–41 http://dx.doi.org/10.1080/00206814.2013.775731.
Sanderson, D.J., Marchini, W.R.D., 1984. Transpression. J. Struct. Geol. 6, 449–458. http://dx.doi.org/10.1016/0191-8141(84)90058-0.
Saul, J., Bruhn, R.L., Forster, C.B., Caine, J.S., Bruhn, R.L., Forster, C.B., 2010. Internal structure, fault rocks, and inferences regarding deformation, fluid flow, and mineralization in the seismogenic Stillwater normal fault, Dixie Valley, Nevada. J. Struct. Geol. 32, 1576–1589. http://dx.doi.org/10.1016/j.jsg.2010.03.004.
Sheldon, H.A., Micklethwaite, S., 2007. Damage and permeability around faults: implications for mineralization. Geology 35, 903. http://dx.doi.org/10.1130/G23860A.1.
Siame, L.L., Bellier, O., 2005. Deformation Partitioning in Flat Subduction Setting: Case of the Andean Foreland of Western Argentina 28° S–24, 1–24 http://dx.doi.org/10.1029/2005TC001787.
Sibson, R.H., 1987. Earthquake rupturing as a mineralizing agent in hydrothermal systems. Geology 15, 701–704.
Sibson, R.H., 1994. Crustal stress, faulting and fluid flow. Geol. Soc. Spec. Publ. 78, 69–84. http://dx.doi.org/10.1144/GSL.SP.1994.078.01.07.
Sibson, R.H., 1996. Structural permeability of fluid-driven fault-fracture meshes. J. Struct. Geol. 18, 1031–1042. http://dx.doi.org/10.1016/0191-8141(96)00032-6.
Sibson, R.H., 2003. Brittle-failure controls on maximum sustainable overpressure in different tectonic regimes. Am. Assoc. Pet. Geol. Bull. 87, 901–908. http://dx.doi.org/10.1306/01290300181.
Sibson, R.H., 2004. Controls on maximum fluid overpressure defining conditions for mesozonal mineralisation. J. Struct. Geol. 26, 1127–1136. http://dx.doi.org/10.1016/j.jsg.2003.11.003.
Sibson, R.H., Moore, J.M.M., Rankin, A.H., 1975. Seismic Pumping a Hydrothermal Fluid Transport Mechanism 653–659. http://dx.doi.org/10.1144/gsjgs.131.6.0653.
Sielfeld, G., Cembrano, J., Lara, L., 2016. Transtension driving volcano-edifice anatomy: insights from Andean transverse-to-the-orogen tectonic domains. Quat. Int. 1–17. http://dx.doi.org/10.1016/j.quaint.2016.01.002.

Suárez, M., Emparan, C., 1997. Hoja Curacautín, región de la Araucanía y del Biobío. Carta geológica de Chile., Servicio N. Carta Geológica de Chile, Servicio Nacional de Geología y Minería.

Tardani, D., Reich, M., Roulleau, E., Takahata, N., Sano, Y., Peréz-Flores, P., Sánchez, P., Cembrano, J., Arancibia, G., 2016. Exploring the structural controls on helium, nitrogen and carbon isotope signatures in hydrothermal fluids along an intra-arc fault system. Geochim. Cosmochim. Acta http://dx.doi.org/10.1016/j.gca.2016.04.031.

Teyssier, C., Tikoff, B., 1998. Strike-slip partitioned transpression of the San Andreas fault system: a lithospheric-scale approach. Geol. Soc. Lond. Spec. Publ. 135, 143–158. http://dx.doi.org/10.1144/GSL.SP.1998.135.01.10.

Teyssier, C., Tikoff, B., Markley, M., 1995. Oblique plate motion and continental tectonics. Geology 23, 447–450. http://dx.doi.org/10.1130/0091-7613(1995)023<0447:OPMACT>2.3.CO;2.

Thiele, R., Lahsen, A., Moreno, H., Varela, J., Vergara, M., 1987. Estudios geológicos regionales a escala 1:100.000 de la hoya superior y curso medio del Biobío.

Tibaldi, A., Lagmay, A.M.F.A., Ponomareva, V.V., 2005. Effects of basement structural and stratigraphic heritages on volcano behaviour and implications for human activities (the UNESCO/IUGS/IGCP project 455). Episodes 28, 158–170.

Tikoff, B., Greene, D., 1997. Stretching lineations in transpressional shear zones: an example from the Sierra Nevada Batholith, California. J. Struct. Geol. 19, 29–39.

Uysal, I.T., Feng, Y., Zhao, J., Bolhar, R., Işik, V., Baublys, K.a., Yago, A., Golding, S.D., 2011. Seismic cycles recorded in late Quaternary calcite veins: geochronological, geochemical and microstructural evidence. Earth Planet. Sci. Lett. 303, 84–96. http://dx.doi.org/10.1016/j.epsl.2010.12.039.

Van Wyk De Vries, B., Merle, O., 1998. Extension induced by volcanic loading in regional strike-slip zones. Geology 26, 983–986. http://dx.doi.org/10.1130/0091-7613(1998)026<0983:EIBVLI>2.3.CO;2.

Veloso, E.E., Anma, R., Yamaji, A., 2009. Ophiolite emplacement and the effects of the subduction of the active Chile Ridge System: heterogeneous paleostress regimes recorded in the Taitao Ophiolite (Southern Chile). Andean Geol. 36, 3–16.

Veloso, E., Gomila, R., González, R., Cembrano, J., Jensen, E., Arancibia, G., 2015. Stress fields recorded on large-scale strike-slip fault systems: effects on the tectonic evolution of crustal slivers during oblique subduction. Tectonophysics 664, 244–255. http://dx.doi.org/10.1016/j.tecto.2015.09.022.

Wang, K., Hu, Y., Bevis, M., Kendrick, E., Robert, S., Vargas, R.B., Lauría, E., Smalley, R., Vargas, R.B., Lauría, E., 2007. Crustal motion in the zone of the 1960 Chile earthquake: detangling earthquake-cycle deformation and forearc-silver translation. Geochem. Geophys. Geosyst. 8, 1–14. http://dx.doi.org/10.1029/2007GC001721.

Weatherley, D.K., Henley, R.W., 2013. Flash vaporization during earthquakes evidenced by gold deposits. Nat. Geosci. 6, 1–5. http://dx.doi.org/10.1038/ngeo1759.

Yamaji, A., 2000. The multiple inverse method: a new technique to separate stresses from heterogeneous fault-slip data. J. Struct. Geol. 22, 441–452. http://dx.doi.org/10.1016/S0191-8141(99)00163-7.

Yamaji, A., Tomita, S., Otsubo, M., 2005. Bedding tilt test for palaeostress analysis. J. Struct. Geol. 27, 161–170.

Yáñez, G., Gana, P., Fernández, R., 1998. Origen y significado geológico de la Anomalía Melipilla, Chile central. Rev. Geol. Chile.

Zhang, Y., Schaubs, P.M., Zhao, C., Ord, A., Hobbs, B.E., Barnicoat, A.C., 2008. Fault-related dilation, permeability enhancement, fluid flow and mineral precipitation patterns: numerical models. Geol. Soc. Lond. Spec. Publ. 299, 239–255. http://dx.doi.org/10.1144/SP299.15.